

REPORT DOCUMENTATION PAGE				AFRL-SR-AR-1R-04-0854	
<small>The public reporting burden for this collection of information is estimated to average 1 hour per response, including the time for gathering and maintaining the data needed, and completing and reviewing the collection of information. Send comments regarding this burden estimate or any other aspect of this collection of information, including suggestions for reducing the burden, to the Department of Defense, Executive Service and Communications Directorate (0704-0188). Respondents should be aware that notwithstanding any other provision of law, no person shall be subject to any penalty for failing to comply with a collection of information if it does not display a currently valid OMB control number.</small>					
PLEASE DO NOT RETURN YOUR FORM TO THE ABOVE ORGANIZATION.					
1. REPORT DATE (DD-MM-YYYY)		2. REPORT TYPE FINAL REPORT		3. DATES COVERED (From - To) 20 JUL 02 - 30 JUN 04	
4. TITLE AND SUBTITLE QUASICRYSTALLINE FILMS FOR TRIBOLOGICAL APPLICATIONS: ROLE OF STOICHIOMETRY, MICROSTRUCTURE, TRANSFORMATION KINETICS, AND OXIDE STRUCTURE AND CHEMISTRY				5a. CONTRACT NUMBER F49620-02-C-0043	
				5b. GRANT NUMBER	
				5c. PROGRAM ELEMENT NUMBER	
				5d. PROJECT NUMBER	
6. AUTHOR(S) DR DAVID PALAITH				5e. TASK NUMBER	
				5f. WORK UNIT NUMBER	
7. PERFORMING ORGANIZATION NAME(S) AND ADDRESS(ES) TECHNOLOGY ASSESSMENT AND TRANSFER 133 DEFENSE HWY, SUITE 212 ANNAPOLIS, MD 21401				8. PERFORMING ORGANIZATION REPORT NUMBER	
9. SPONSORING/MONITORING AGENCY NAME(S) AND ADDRESS(ES) AFOSR/NL 4015 WILSON BLVD., ROOM 713 ARLINGTON, VA 22203-1954				20040715 132	
12. DISTRIBUTION/AVAILABILITY STATEMENT APPROVE FOR PUBLIC RELEASE: DISTRIBUTION UNLIMITED					
13. SUPPLEMENTARY NOTES					
14. ABSTRACT Significant progress was made towards an understanding of phase development and oxidation in the AlCuFe quasicrystalline system. Microstructure analysis by synchrotron diffraction exhibited the route for phase formation from the as-deposited precursor films. Formation of the R-phase occurred at 450 degree, below the previously published value of 475 degree. Preferential oxidation occurs in the near-surface region and temporarily disrupts formation of the R-phase microstructure, despite encapsulation in argon atmosphere. Fluctuation microscopy and other structural analysis showed the presence of an ordered, polycrystalline oxide on the surface of AlCuFe films annealed at 500 degree to 600 degree. This oxide film appeared to consist of aluminum oxide, and lacked copper and iron. The combination of microstructure analysis, phase development on annealing, and analysis of the oxide phase provided fundamental understanding of AlCuFe quasicrystalline coatings in steam engine applications. A tribological testing system capable of operating in a high temperature, steam environment was modified and tested. Room ambient and 100 degree steam					
15. SUBJECT TERMS					
16. SECURITY CLASSIFICATION OF:			17. LIMITATION OF ABSTRACT	18. NUMBER OF PAGES	19a. NAME OF RESPONSIBLE PERSON
a. REPORT	b. ABSTRACT	c. THIS PAGE			19b. TELEPHONE NUMBER (Include area code)

BEST AVAILABLE COPY

Testing of Sb-impregnated graphit-hard ceramic combinations supported the high temperature steam test results at Enginon.

**BEST AVAILABLE COPY**

**QUASICRYSTALLINE FILMS  
FOR TRIBOLOGICAL APPLICATIONS:  
Role Of Stoichiometry, Microstructure, Transformation Kinetics,  
And Oxide Structure And Chemistry**

**DRAFT FINAL REPORT**

**AFOSR Contract No. F49620-02-C-0043**

Submitted to:  
**Lt. Col. Paul Trulove  
Air Force Research Laboratory  
AFOSR/NL  
4015 Wilson Blvd.  
Arlington, VA 22203**

Submitted by:  
**Dr. Larry Fehrenbacher  
Technology Assessment and Transfer  
133 Defense Hwy. Suite 212  
Annapolis, MD 21401**

**June 30, 2004**

**DISTRIBUTION STATEMENT A**  
Approved for Public Release  
Distribution Unlimited

## TABLE OF CONTENTS

Section	Title	Page
1	Program Objectives	1
2	Research Results	2
3	Steam Engine Tribology	27
4	Summary Conclusions	44
5	Publications	44

### 1. PROGRAM OBJECTIVES

There were five program objectives:

**1.1 Objective 1** The first objective of the program was to examine the limits of the oxygen uptake and related stability of the icosahedral phase in AlCuFe films. Achieving this objective required a series of post-annealing treatments at temperatures of 500°C for different hold times under both vacuum and air environments. The compositions including the amount of oxygen in the bulk of the film were measured by X-ray Photoelectron Spectroscopy (XPS) ion beam profiling. The depth and composition of the surface oxide layers were measured using the same method. The presence of impurity diffusion from the substrate also was quantified. This helped to determine the potential service conditions that dictate the use of an interlayer diffusion barrier. The icosahedral and cubic phase distributions of all the annealed samples were determined by laboratory and synchrotron x-ray diffraction analysis. Since as-sputtered films require high temperature annealing treatments to convert them to stable quasicrystalline structures, annealing kinetics that control the conversion of AlCuFe films to the icosahedral phase were studied using hot stage x-ray and electron diffraction techniques.

**1.2 Objective 2** The second objective was to conduct in depth investigation of the chemistry, microstructure, and phase character of the oxide layers in an attempt to correlate it with the underlying phase and microstructure of the bulk. A combination of high-resolution cross-section electron microscopy (HREM), synchrotron grazing incident scattering (GIXS), and focused ion beam (FIB) slicing of the transmission electron spectroscopy (TEM) samples of near surface regions of carefully selected samples were used. A newly developed method, Fluctuation Microscopy (FM) was also employed to characterise the chemistry and structure of the surface and near surface oxide layers.

**1.3 Objective 3** The third objective was to determine the relationship between icosahedral AlCuFe films and surface energy, microhardness, and friction properties as a function of the oxygen content of the icosahedral phase. This objective required that the XPS compositional, oxide layer thickness, and XRD data to be correlated with measurements of the dispersive and polar components of the surface energy, microhardness, and friction coefficients. These correlations helped define the limits and capabilities of high oxygen containing icosahedral films versus low oxygen containing films.

**1.4 Objective 4 (Optional objective contingent on supplementary funding)** The fourth objective was to demonstrate the performance capabilities of AlCuFe icosahedral films in simulated application environments such as non-stick and fretting wear applications in aircraft turbine engines. Examples applications include variable stator vane bushings, blade (dovetail) roots, and wear seals. Also, magnetron sputtered icosahedral coated titanium alloy and steel substrates were used to test adhesion and corrosion resistance. These results will help to determine the potential of magnetron AlCuFe films for specific applications.

**1.5 Objective 5** The fifth and final objective was to explore low-friction, low-wear thin film coating systems for use in steam engine environments with steam temperatures to 600°C. Friction and wear testing of thin films under these conditions presented major technical challenges. Few high temperature tribometers exist anywhere in the world, and even fewer operate under a steam environment. TA&T possessed a tribometer that could be modified to meet these conditions. The basic unit was developed by Dr. Michael Gardos for high temperature tribological measurements. It consists of a rotating sample and rub block, and allows measurement of the normal force, the frictional force, the temperature, and the in situ wear rate in real time – a truly unusual measurement capability. Prior to the work reported on here, TA&T had already modified this tribometer to perform real time studies of the effects of corrosion on friction and wear specimens in a salt spray environment. TA&T then modified the system under this contract to permit friction and wear measurements in a high temperature steam environment in order to expedite development of thin film material systems for steam engine applications.

## **2. RESEARCH RESULTS**

In this section, results of research directed toward achieving Objectives 1 – 3 are presented. The major portion of the analysis was performed under a subcontract to the University of Michigan under the direction of Dr. John Bilello. The work was performed by Dr. Matthew Daniels.<sup>1</sup> Film preparation including annealing, and preliminary evaluation was performed by Technology Assessment and Transfer.

**2.1 Film Preparation** An AlCuFe powder pressed target was used to deposit 10 µm coatings by RF sputtering in the cylindrical planar magnetron sputter system. A study of the target was recently submitted. The base pressure prior to sputtering was  $3 \times 10^{-7}$  Torr. Sputtering was performed at 600 W (800 V) in 5 mTorr argon sputter gas pressure with a target-to-substrate distance of 6 cm. No substrate bias was applied for these depositions and substrates were not otherwise heated.

Coated alumina substrates were annealed by the quartz encapsulation method with 500 mT argon gas and annealed in a box furnace. The conditions for these anneals are summarized in Table 1. For anneals performed at 450°C, 500°C, and 550°C, the observed rates of heating between 200°C and 400°C were  $\approx 1.2^\circ\text{C}\cdot\text{sec}^{-1}$ ,  $\approx 2.0^\circ\text{C}\cdot\text{sec}^{-1}$ , and  $\approx 2.6^\circ\text{C}\cdot\text{sec}^{-1}$ , respectively. Cooling was performed by quenching encapsulated samples in liquid nitrogen, or by cooling in air. Liquid nitrogen quench of an ampoule resulted in a cooling rate of the sample of  $\approx 2.9^\circ\text{C}\cdot\text{sec}^{-1}$  from 400°C to 200°C. Cooling an ampoule in air resulted in a cooling rate of  $\approx 1.1^\circ\text{C}\cdot\text{sec}^{-1}$  from 400°C to 200°C.

---

<sup>1</sup> Daniels, M., "Phase, Microstructure, and Chemistry of AlCuFeCr and AlCuFe Quasicrystalline Wear Coatings Produced Via Physical Vapor Deposition," Dissertation submitted in partial fulfillment of the requirements for a Ph.D., Materials Science, University of Michigan, 2003.

**Table 1. Summary of film anneal conditions (LN quench refers to quenching of a sample in ampoule in liquid nitrogen).**

Sample	Anneal Method	Cooling Method	Temp. (°C)	Time (hrs)
A1	ampoule	LN quench	550	10
A2	ampoule	LN quench	550	1
A3	ampoule	LN quench	500	2
A4	ampoule	LN quench	500	1
A5	ampoule	LN quench	450	10
A6	ampoule	LN quench	450	2
A7	ampoule	LN quench	450	1
A8	unannealed			
A9	ampoule	LN quench	500	60
A10	ampoule	LN quench	450	1.5
B1	ampoule	air quench	550	10
B2	ampoule	air quench	550	1
B3	ampoule	air quench	500	1
B4	ampoule	air quench	450	10

## 2.2 Microstructure Analysis by Synchrotron X-ray Diffraction

In the AlCuFe system, the rhombohedral approximant (R-phase) ( $a=32.16 \text{ \AA}$ ,  $\alpha=36^\circ$ ) similar to the I-phase phase has been shown to exist below  $675^\circ$ .<sup>2</sup> Due to its close structural similarity with the I-phase, the R-phase is expected to show a similar degree of hardness and coefficient of friction to that of the I-phase. Several studies have focused on the difference between I-phase and the R-phase<sup>3,4,5,6</sup> and have shown an increase in the measured widths of the (18,29) and (20,32) peaks and in characteristic splitting of (6,9), (7,11), and (8,12) I-phase peaks using the Cahn indexing scheme.<sup>7</sup> However, grain growth and phase development of the R-phase from its nanoquasicrystalline precursor has never been studied.

Many other crystalline structures have been characterized in the AlCuFe system in addition to the R-phase approximant. The mechanical properties and wear characteristics of these phases are not well known. They commonly have lattice parameters similar to those of the R-phase. Some of these phases include the  $\beta$  ( $\text{Al}_{53.7}\text{Cu}_{13.1}\text{Fe}_{33.2}$ ),  $\tau$  ( $\text{Al}_{47.5}\text{Cu}_{48}\text{Fe}_{4.5}$ ), and  $\lambda$  ( $\text{Al}_{73.4}\text{Cu}_{5.1}\text{Fe}_{21.5}$ ) phases, which also exhibit diffraction peaks between the (18,29) and (20,32) peaks of the R-phase.<sup>8,9,10</sup> The aluminum-deficient  $\beta$  phase is a common impurity in the AlCuFe system, and has been observed in plasma sprayed coatings<sup>11,12</sup> and annealed I-phase powders<sup>13</sup> as a result of preferential aluminum oxidation.

- <sup>2</sup> M. Audier and P. Guyot, Proceedings of the Third International Meeting on Quasicrystals, Vista Hermosa, Mexico (1989) 152.
- <sup>3</sup> A. Waseda, K. Araki, K. Kimura, H. Ino, J. Non-Cryst. Solids, 153&154 (1993) 635.
- <sup>4</sup> F. Dénoyer, P. Launois, T. Motsch, M. Lambert, J. Non-Cryst. Solids, 153&154 (1993) 595.
- <sup>5</sup> D. Gratias, Y. Calvayrac, J. Devaud-Rzepski, F. Faudot, M. Harmelin, A. Quivy, P. A. Bancel, J. Non-Cryst. Solids 153&154 (1993) 482.
- <sup>6</sup> K. Edagawa, A. Waseda, K. Kimura, H. Ino, Mat. Sci. and Eng. A, 134 (1991) 939.
- <sup>7</sup> J. W. Cahn, D. Shechtman, D. Gratias, J. Mater. Res., 1 (1) (1986) 13.
- <sup>8</sup> J. M. Dubois, S. S. Kang, J. von Stebut, J. Mat. Sci. Lett. 10 (1991) 537.
- <sup>9</sup> P. J. Pinhero, J. W. Anderegg, D. J. Sordet, M. F. Besser, P. A. Thiel, Phil. Mag. B, 79, 1 (1999) 91.
- <sup>10</sup> S. M. Lee, H. J. Jeon, B. H. Kim, W. T. Kim, D. H. Kim, Mat. Sci. and Eng. A, 304-306 (2001) 871.
- <sup>11</sup> D. J. Sordet, M. J. Kramer, I. E. Anderson, M. F. Besser, Proc. of the Fifth International Meeting on Quasicrystals, (1991) 778.

In this work, the microstructural development during annealing from an as-deposited nanoquasicrystalline PVD coating to the rhombohedral approximant phase (R-phase) in the AlCuFe system is discussed. Magnetron sputtering was used to deposit 10  $\mu\text{m}$  coatings on sintered alumina substrates from a powder composite target resulting in an amorphous or nanoquasicrystalline precursor. Films were subsequently annealed in quartz ampoules for a variety of times and temperatures and characterized using synchrotron x-ray diffraction, and sputter depth profiling with XPS. Anneals were performed at 450°C to 550°C to ensure that the R-phase was formed below the reported icosahedral phase (I-phase) transition at 675°C. One anneal was also performed at 850°C to compare these results with the icosahedral phase. Annealing at 450°C for 1 hour showed partial conversion to R-phase, with  $\beta$  phase also present as a result of aluminum depletion caused by preferential oxidation and enrichment at the surface of the film.

The synchrotron diffraction pattern from an unannealed sample is shown in Figure 1. Similar diffraction patterns have been observed for samples in the AlCuFe system,<sup>14,15,16</sup> and also coatings in the AlCuFeCr system.<sup>17</sup> The full diffraction pattern of A5 is shown in Figure 2 as a schematic for comparison against other patterns of the icosahedral phase and the R-phase. Boxed regions in Figure 2 show the limited portions of the diffraction pattern that were scanned for all samples, including the location of expected impurity phases between the two prominent peaks at  $2\theta \approx 35^\circ$ . A portion of the diffraction pattern from A7 is compared against that of an unannealed sample in Figure 3, and also against the diffraction pattern from other samples in this study annealed at 450°C in Figure 4. Anneals performed at 450°C (A10, A7, A6, A5) were particularly useful because the diffusion kinetics of the reaction were slowed. Several sharp peaks were found to emerge from the background, corresponding to the developing R-phase and  $\beta$  phases. Examination of the background shows that it no longer resembles the one broad maximum observed in the unannealed film. Instead, splitting is observed, and the intensity is concentrated around the base of the peaks from the R-phase. This behavior suggests that this process is related to grain growth from nanoscale and/or heavily defected R-phase grains in the unannealed film, rather than a phase transformation from an amorphous structure, as previously suggested.<sup>23,24,25</sup>

- 
- <sup>12</sup> M. F. Besser, D. J. Sordet in *New Horizons in Quasicrystals: Research and Applications*, Ames, Iowa (1996) 288.
  - <sup>13</sup> D. J. Sordet, L. A. Gunderman, M. F. Besser in *New Horizons in Quasicrystals: Research and Applications*, Ames, Iowa (1996) 296.
  - <sup>14</sup> R. Haberkern, C. Roth, R. Knöfler, L. Schulze, P. Häussler, *Mat. Res. Soc. Symp. Proc.* 553 (1999) 13.
  - <sup>15</sup> C. Roth, G. Schwalbe, R. Knöfler, F. Zavaliche, O. Madel, R. Haberkern, P. Häussler, *J. Non-Cryst. Solids*, 252 (1999) 869.
  - <sup>16</sup> C. Madel, G. Schwalbe, R. Haberkern, P. Häussler, *Mat. Sci. and Eng. A* 294-296 (2000) 535.
  - <sup>17</sup> M. J. Daniels, J. Maciejewski, J. S. Zabinski, Z. U. Rek, S. M. Yalisove, J. C. Bilello, *Mat. Res. Soc. Symp. Proc.*, 643 (2001) K 8.4.1.
-

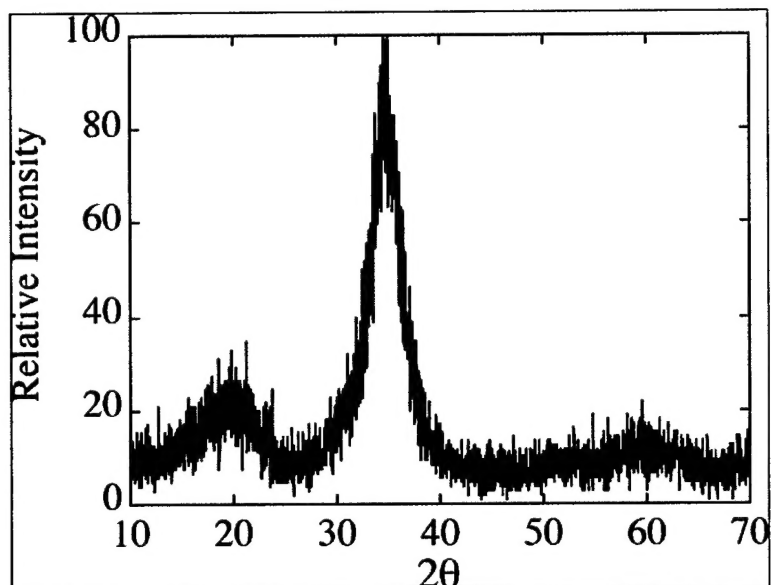


**Figure 1.** Asymmetric diffraction pattern of an unannealed AlCuFe coating formed by sputter deposition. Sampling depth of the x-ray beam was approximately 1.7  $\mu\text{m}$ .

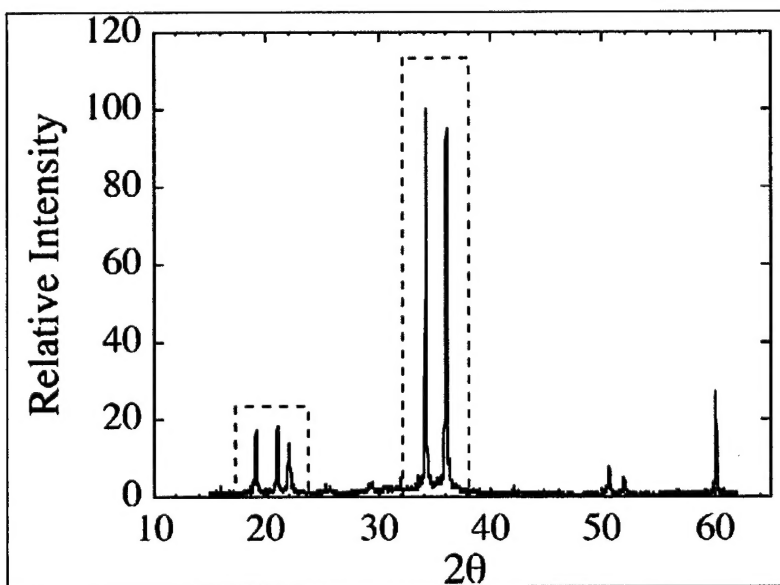


**Figure 2.** Full diffraction pattern from an R-phase film annealed at 450°C for 10 hours and quenched in liquid nitrogen (A5). Boxed regions show portions of the pattern that are displayed for all samples. ( $\lambda=1.240 \text{ \AA}$ )



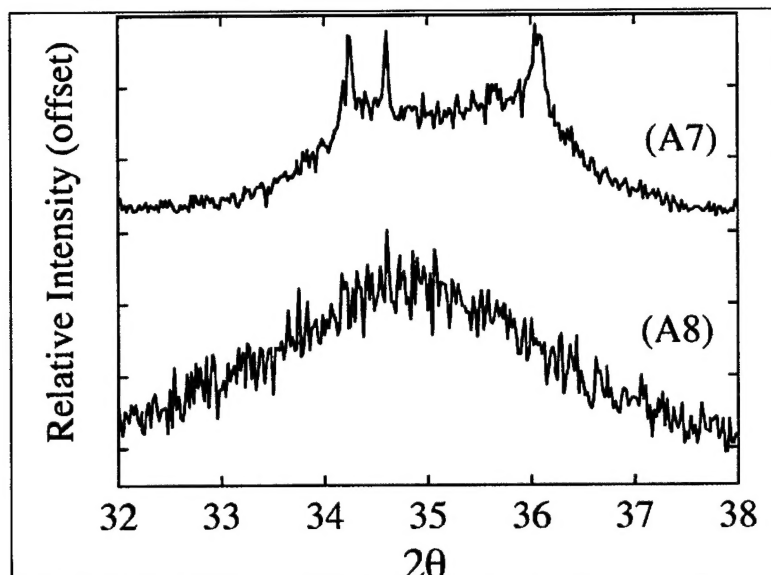


**Figure 3.** Selected region of the diffraction pattern ( $\lambda=1.240 \text{ \AA}$ ) from a sample annealed at  $450^\circ\text{C}$  for 1 hour and liquid nitrogen quenched (A7) against an unannealed sample (A8), enlarged to compare their structures. Sampling depth of the x-ray beam was  $1.7 \text{ }\mu\text{m}$ .

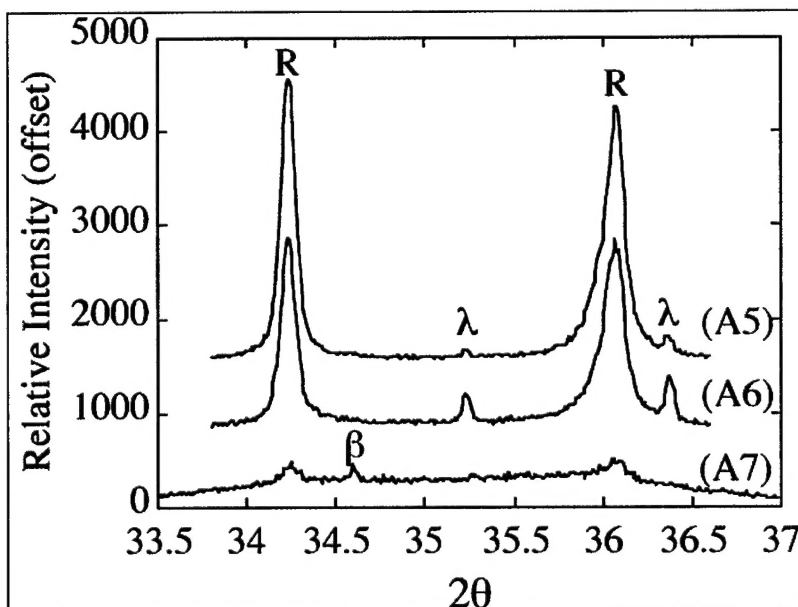


**Figure 4.** Selected region of the diffraction pattern from a sample annealed at  $450^\circ\text{C}$  for 1 hour and liquid nitrogen quenched (A7) against samples annealed at  $450^\circ\text{C}$  for 2 hours (A6) and 10 hours (A5), enlarged to compare their structures. Sampling depth of the x-ray beam was  $1.7 \text{ }\mu\text{m}$ .

Observation of the intermediate stage of microstructure development in sample A7 led to production and analysis of another sample in the intermediate stages of annealing, sample A10, annealed in a quartz ampoule for 1.5 hours. It was hypothesized during analysis of A7 that the development of the  $\beta$  phase was correlated to the selective oxidation and leaching of aluminum from the film, producing the aluminum-deficient  $\beta$  phase near the surface. This theory was tested using a depth profile performed on A10 at 8 keV to examine the structure at different penetration depths and elucidate microstructure development in the film. This data is shown in Figure 5. Progressive scanning of the film at different incident angles (and therefore, penetration depths) showed predominantly  $\beta$  phase at the surface of the film, while scans of the bulk showed a well-developed R-phase structure.

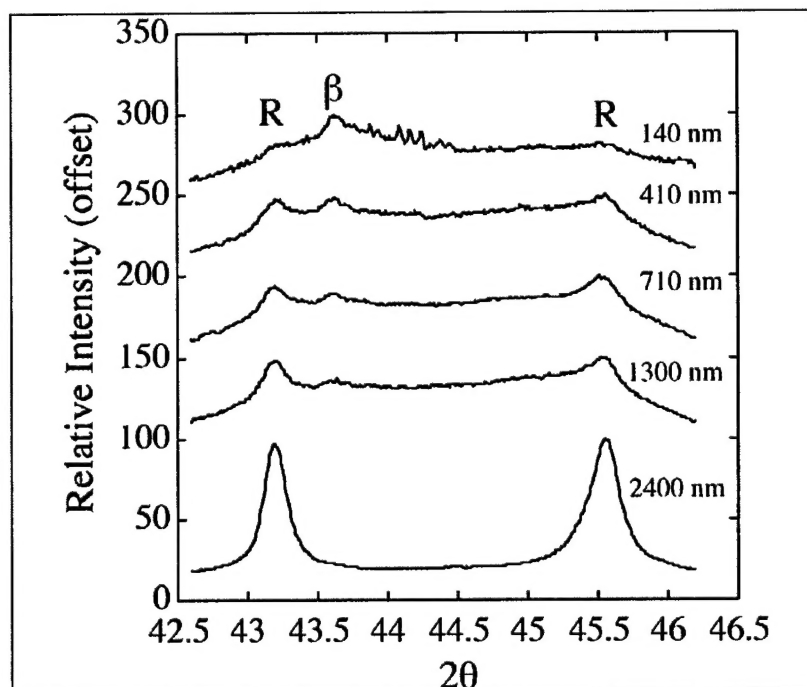


**Figure 5.** Selected region of the diffraction pattern from a sample annealed at 450°C for 1.5 hours and liquid nitrogen quenched (A10) shown as a function of penetration depth. Various penetration depths were achieved by varying the incident angle of the x-ray beam on the surface of the film. The  $\beta$  phase is dominant at the surface, unlike the AlCuFeCr system, where crystalline aluminum nucleated at the surface. The R-phase is dominant in the bulk, below 1000 nm. Note that this scan was performed at an incident energy of 8 keV, corresponding to a wavelength of 1.550 Å. This  $2\theta$  region shown is analogous to the region shown in Figure 4, analyzed using a different wavelength.

With the observation of  $\beta$  phase development at the surface of A10, the evolving model of the microstructure formation on annealing becomes clear. Correlation with the XPS depth profiles from A7 and A5 (discussed in Section 2.3) give further evidence to form a model. Localized aluminum-deficient regions developed in the near surface region of films during the first stages of annealing due to surface enrichment and preferential oxidation of aluminum, with accompanying depletion from the bulk. Additional annealing caused diffusion of aluminum from the bulk towards the surface of the film, broadening the aluminum profile in sample A5. This aluminum diffusion also served to compensate for

the aluminum deficiency that caused formation of the  $\lambda$  phase in the near surface region. The result was a disappearance of the  $\beta$  phase in all anneals longer than 1.5 hours. As annealing progressed, aluminum diffusion continued, producing a secondary  $\lambda$ - $\text{Al}_{13}\text{Fe}_4$  (aluminum-rich) phase in slightly longer anneals (A6, 2hrs, 450°C). It is currently unresolved whether this impurity phase appears near the surface as a result of continued aluminum diffusion, or whether it appears merely as a result of localized aluminum-rich regions throughout the film. This  $\lambda$  impurity was also removed by further annealing and diffusion.

The  $18 \leq 2\theta \leq 23$  and  $33.5 \leq 2\theta \leq 37$  regions of the diffraction pattern for all ampoule anneals quenched in liquid nitrogen are shown in Figures 6 and 7, respectively. The analogous x-ray diffraction patterns for ampoule anneals cooled in air are shown in Figures 8 and 9, respectively. All samples were deposited on the same type of substrate in the same deposition system and analyzed in the same x-ray system, therefore, counts can be compared instead of a normalized intensity to show development of the structure. Qualitatively, intensity of both (18,29) and (20,32) peaks increased with longer anneals and at greater temperatures. The  $\beta$  impurity observed in A7 was also observed in A10, and has already been discussed, but this phase was not observed in any other ampoule anneal. The full width at half-maximum (FWHM) of the (18,29) peak was measured as an indicator of grain size and crystal perfection produced by a variety of anneal times, anneal temperatures, and cooling rates. This data is summarized in Table 2. A number of comparisons were made between the various anneal conditions and the measured FWHM. Measurement error in the FWHM was estimated to be 20% of the FWHM of the standard, or  $0.006^\circ$  in this instance. Given this method of error estimation, the FWHM of all samples presented in Table 2 are statistically similar. The FWHM presented here indicate no change in either crystal perfection or enlarged grains due to the various annealing conditions. Once the R-phase was fully formed (A6, 450°C, 2 hrs), the FWHM was essentially unchanged by further annealing, or annealing at higher temperatures. Moreover, the decrease in cooling rate produced by quenching in air versus liquid nitrogen ( $1.1^\circ\text{C}\cdot\text{sec}^{-1}$  and  $2.9^\circ\text{C}\cdot\text{sec}^{-1}$ , respectively) produces a small to negligible increase in the FWHM. To summarize, once the R-phase has fully developed, further changes in crystallite size and perfection, if any, produce small to negligible changes in the FWHM of the (18,29) peak. In addition, in the range between the two cooling rates investigated in this work, structural stability of the R-phase is demonstrated to be independent of cooling rate.

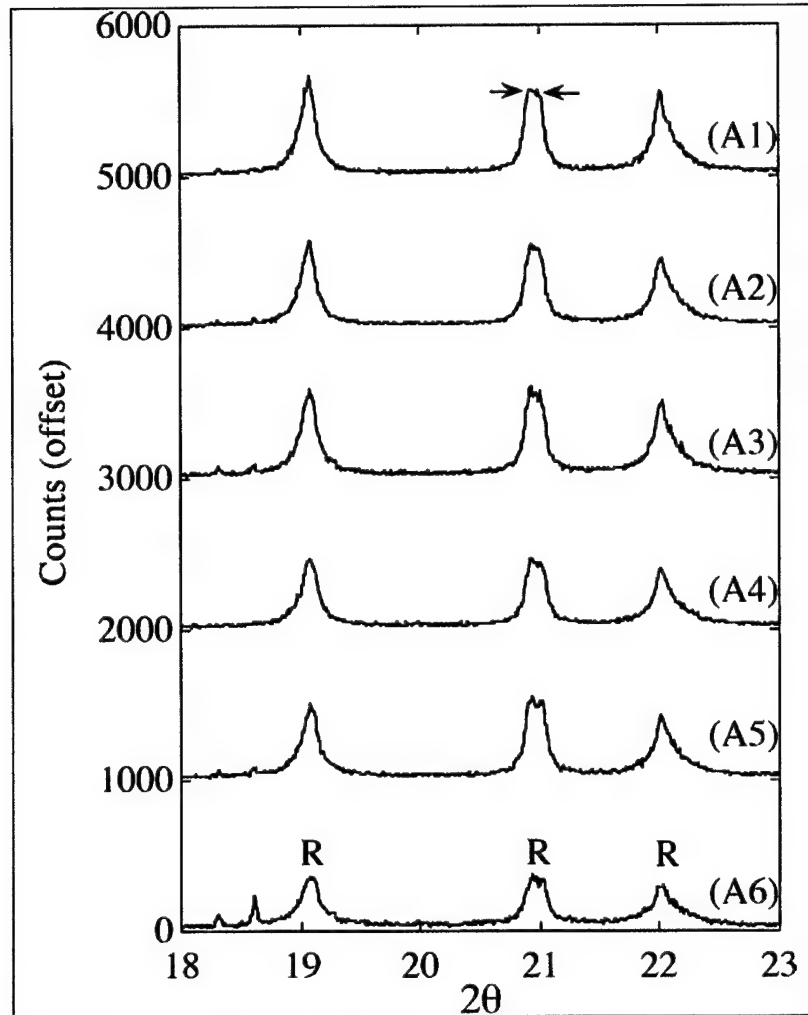


**Figure 6.** Diffraction patterns showing raw counts as a function of various ampoule heat treatments quenched in liquid nitrogen. The heat treatments were 550°C, 10 hr (A1); 550°C, 1 hr (A2); 500°C, 2 hr (A3); 500°C, 1hr (A4); 450°C, 10 hr (A5); and 450°C, 2 hr (A6). Arrows show peak splitting indicative of the rhombohedral phase. Sampling depth of the x-ray beam was  $1.7 \mu\text{m}$ . ( $\lambda=1.240 \text{ \AA}$ )

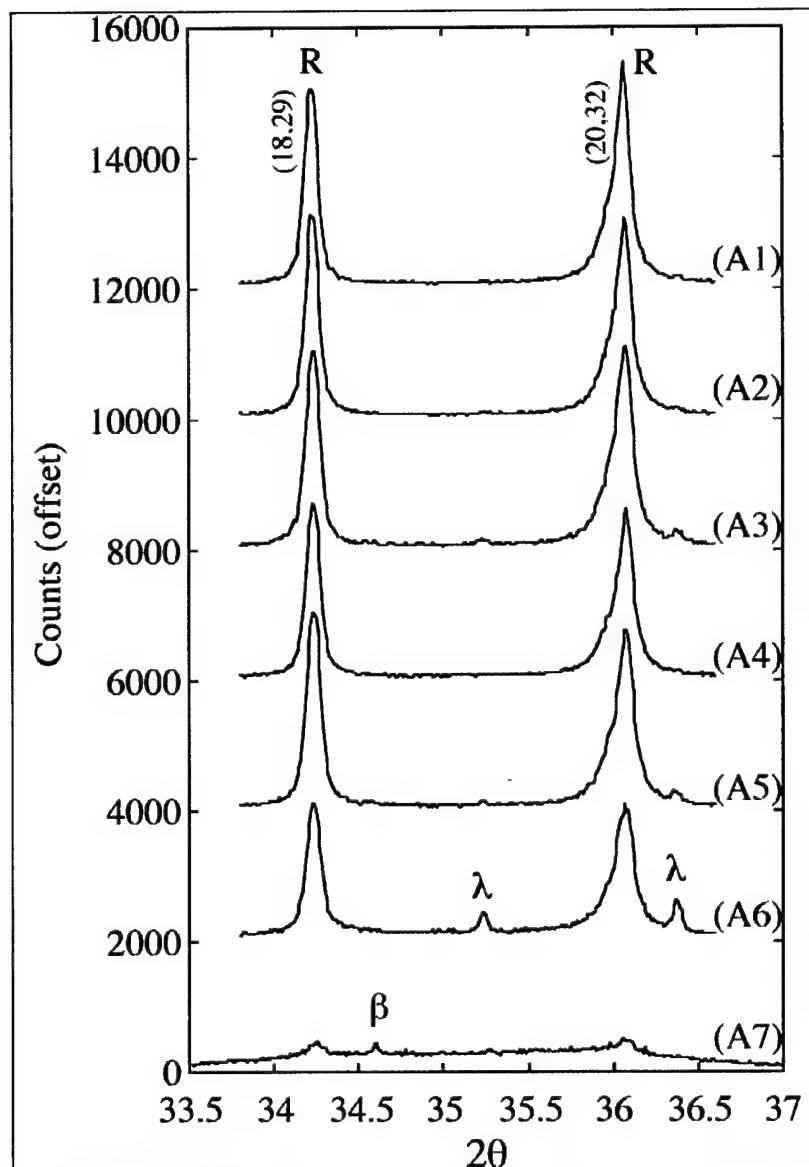


**Figure 7.** Diffraction patterns showing raw counts as a function of various ampoule heat treatments quenched in liquid nitrogen. The heat treatments were 550°C, 10 hr (A1); 550°C, 1 hr (A2); 500°C, 2 hr (A3); 500°C, 1hr (A4); 450°C, 10 hr (A5); 450°C, 2 hr (A6); and 450°C, 1 hr (A7). Sampling depth of the x-ray beam was 1.7  $\mu\text{m}$ . ( $\lambda=1.240 \text{ \AA}$ )

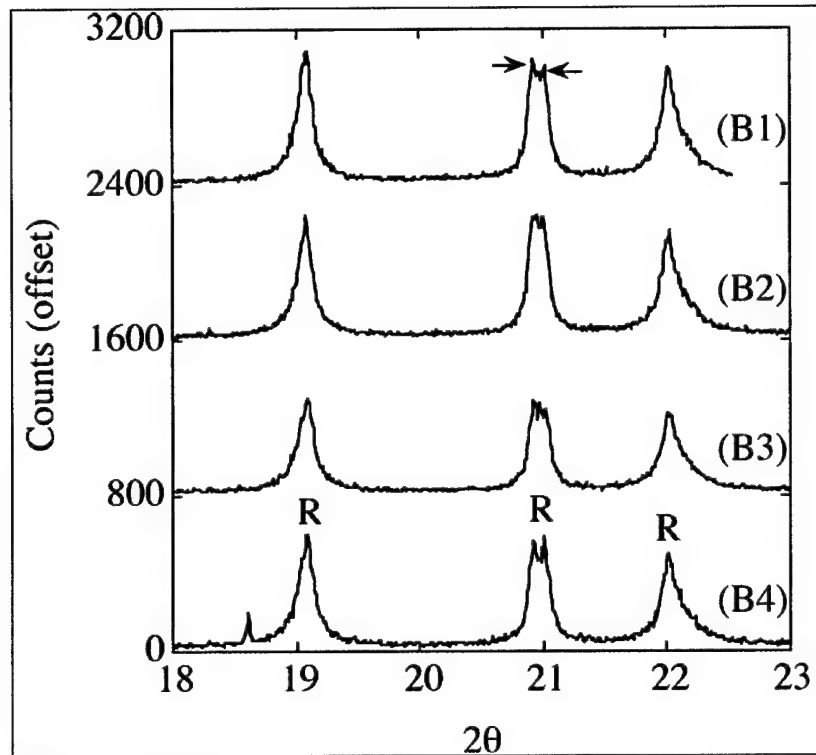


**Figure 8.** Diffraction patterns showing raw counts as a function of various ampoule heat treatments followed by air cool. The heat treatments were 550°C, 10 hr (B1); 550°C, 1 hr (B2); 500°C, 1 hr (B3); 450°C, 10 hr (B4). Arrows show peak splitting due to formation of the rhombohedral phase. Sampling depth of the x-ray beam was 1.7  $\mu\text{m}$ . ( $\lambda=1.240 \text{ \AA}$ )

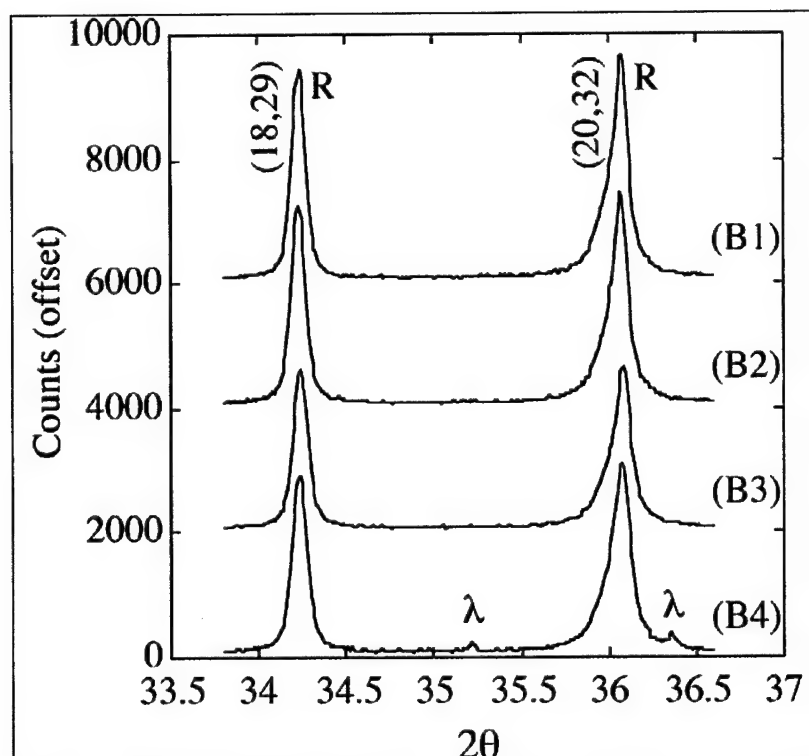


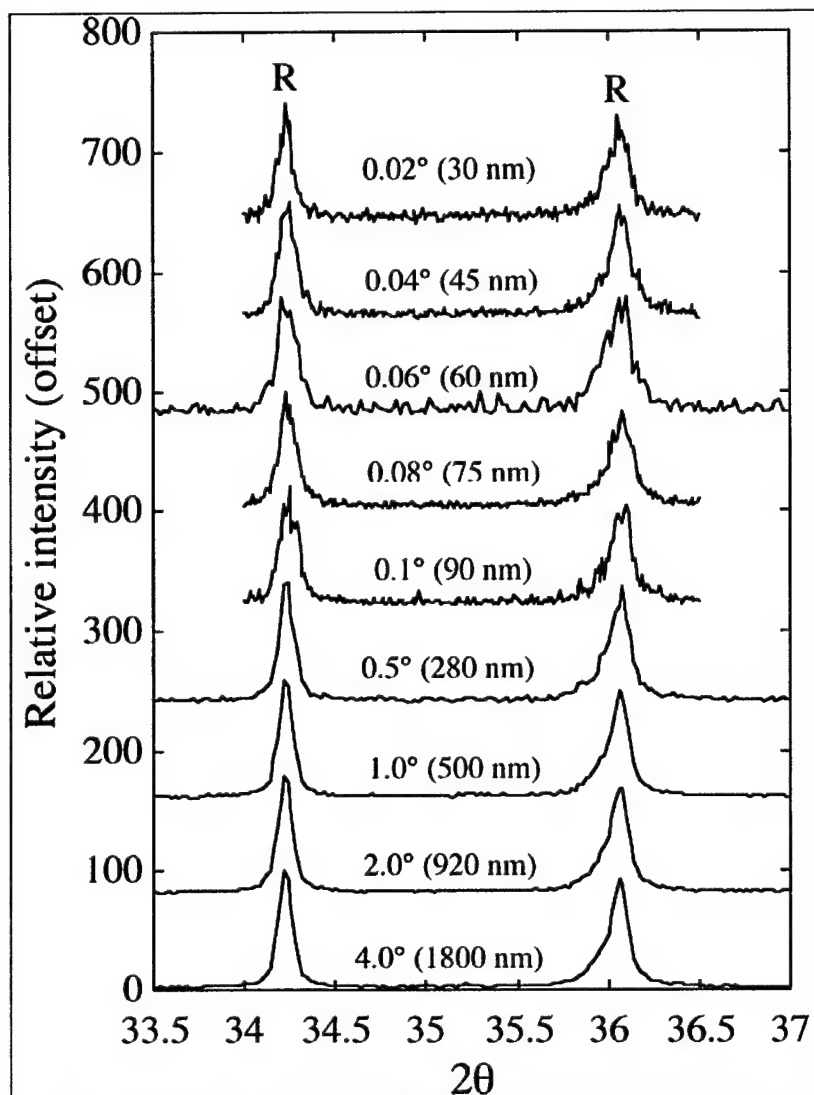
Figure 9. Enlarged region of the diffraction patterns showing raw counts as a function of various ampoule heat treatments followed by air cool. The heat treatments were 550°C, 10 hr (B1); 550°C, 1 hr (B2); 500°C, 1 hr (B3); 450°C, 10 hr (B4). Sampling depth of the x-ray beam was 1.7  $\mu\text{m}$ . ( $\lambda=1.240 \text{ \AA}$ )

Table 2. Comparison of peak widths of (18,29) peak from the rhombohedral approximant phase

Sample	Anneal Method	Cooling Method	Anneal Temp. (°C) /Time (hrs)	FWHM of (18,29) peak
A6	ampoule	LN quench	450/2	0.094±0.006
A5	ampoule	LN quench	450/10	0.095±0.006
B4	ampoule	air cool	450/10	0.097±0.006
A4	ampoule	LN quench	500/1	0.087±0.006
B3	ampoule	air cool	500/1	0.095±0.006
A2	ampoule	LN quench	550/1	0.087±0.006
B2	ampoule	air cool	550/1	0.093±0.006
A1	ampoule	LN quench	550/10	0.089±0.006
B1	ampoule	air cool	550/10	0.091±0.006

X-ray scans performed as a function of depth on Sample A9 (500°C, 60 hours) are also shown in Figure 10. This sample was tested in order to show both the long-term stability of the R-phase at 500°C, and also to detect any oxide phases that were present at the surface of this R-phase film. It was

demonstrated in sample A10 that a  $\beta$  impurity developed in the aluminum-deficient regions during the initial stages of annealing. It was believed that further compositional redistribution may have continued during prolonged annealing, producing  $\lambda$  or  $\beta$  impurities. In order to test for further secondary phase development, A9 was subjected to depth profiling with the synchrotron x-ray beam. No crystalline oxide phases or other impurities were observed at any penetration depth. As a result, further localized compositional variations in the film significant enough to cause secondary phase formation are conclusively excluded. The oxide layer and enriched aluminum region present at the surface must therefore exist either as an amorphous structure, or in quantities insufficient to cause detection on the x-ray diffraction pattern.



**Figure 10.** Enlarged region of the diffraction pattern from sample A9 (annealed at 500°C for 60 hours in ampoule and quenched in liquid nitrogen), taken as a function of incident angle (and corresponding calculated depth) to show that the R-phase structure is present throughout the thickness of the film to a depth of 1800 nm. ( $\lambda=1.240 \text{ \AA}$ )



In addition to the samples annealed directly into the rhombohedral approximant phase, one sample was annealed at 850°C in order to form the true icosahedral quasicrystalline phase. The diffraction patterns as a function of depth for this sample are shown in Figure 11. Enlargement of the surface and bulk diffraction patterns are also compared directly in Figure 12. While the single-phase rhombohedral approximant is formed below 600°C, this is not the case for the quasicrystalline phase at high temperature. In the near-surface region, the aluminum-deficient  $\beta$  phase dominates the microstructure. While this phase appeared as a transient state in the development of the rhombohedral approximant phase, in the icosahedral microstructure, this phase is formed at the surface. Several other impurity phases are also present through the depth, however, these phases are not well characterized, and may be oxide products or contaminants.

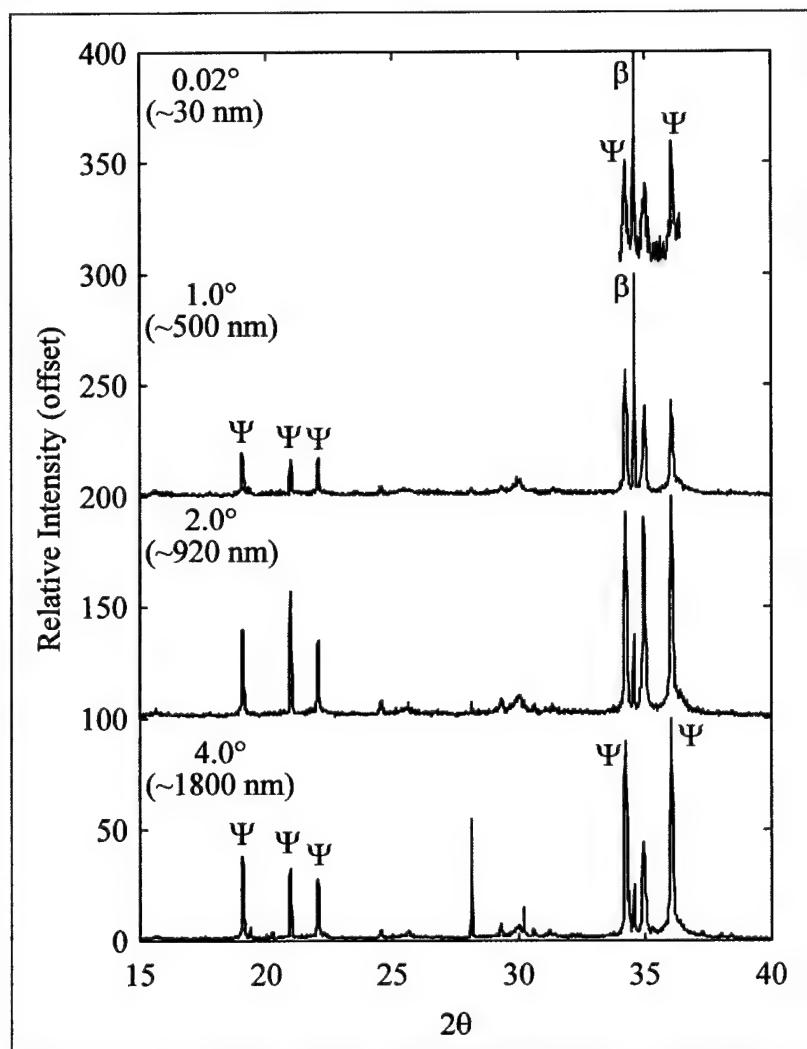


**Figure 11.** Depth profile synchrotron diffraction patterns for a sample annealed at 850°C for 5 hours, showing the predominantly beta ( $\beta$ ) structure at the surface, and the icosahedral ( $\Psi$ ) phase in the bulk

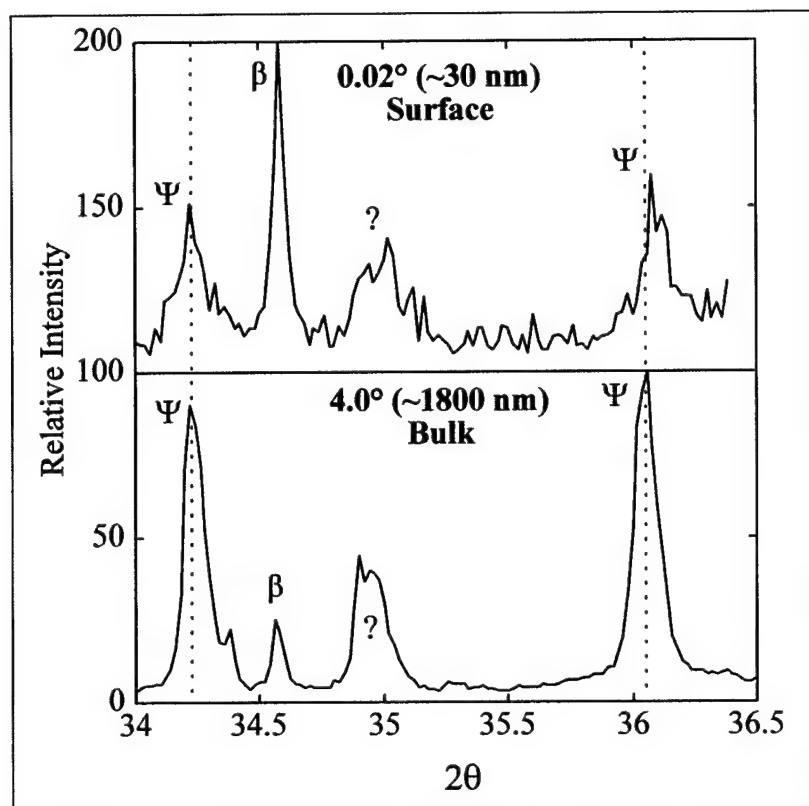


**Figure 12. Enlargement and direct comparison of the diffraction patterns from the surface (30 nm) and bulk (1800 nm).**

This microstructural development of AlCuFe PVD films during annealing is then summarized as follows. During the initial stages of annealing at 450°C, oxidation and aluminum enrichment at the surface of the film created an aluminum-deficient region (in comparison to R-phase) where a  $\beta$  structure developed. Further annealing caused diffusion of aluminum towards the surface of the film, which compensated for the aluminum deficiency and caused disappearance of the  $\beta$  phase. In certain regions, the  $\lambda$  (aluminum-rich) phase also formed. This phase was also removed with further annealing. Upon complete formation of the R-phase, the structure is stable and is not subject to further impurity phase development. Annealing at 500°C and 550°C causes diffusion to occur more quickly, causing full R-phase development in less than 1 hour. Annealing at 850°C causes icosahedral quasicrystalline phase development. However, formation of several impurity phases also occurs. Comparison of anneals at 450, 500, 550, and 850°C does suggest that the region of phase stability may be larger for the R-phase than for the true quasicrystalline structure.

**2.3 Sputter Profile XPS** Composition analysis was performed in an x-ray photoelectric spectroscopy (XPS) system operated at a pressure of  $(8 \times 10^{-10})$  Torr. Relative concentrations in film samples were estimated using sensitivity factors determined from elemental standards and the aluminum 2p, copper 2p<sub>3/2</sub>, iron 2p<sub>3/2</sub>, chromium 2p<sub>3/2</sub>, and oxygen 1s XPS spectra. While elemental sensitivity factors have been used in XPS<sup>18</sup> and Auger<sup>19</sup> studies of quasicrystalline structures, it should be noted that their

<sup>18</sup> S. Suzuki, Y. Waseda, N. Tamura, K. Urban, Scripta Mat. 35 (1996) 891.

<sup>19</sup> C. J. Jenks, J. W. Burnett, D. W. Delaney, T. A. Lograsso, P. A. Thiel, Appl. Surf. Science 157 (2000) 23.

use may lead to errors of several atomic percent.<sup>20</sup> Binding energy positions were calibrated using the gold 4f7/2 peak at 83.93 eV, and the copper 3s and copper 2p3/2 peaks at 122.39 and 932.47 eV, respectively. A monochromated aluminum K $\alpha$  x-ray beam with a 300  $\mu$ m spot size was used for analysis. Synchrotron depth profiling has been used extensively in this work to characterize structure as a function of depth. In instances where an oxide or oxygen-stabilized phase forms near the termination surface of the film, it is frequently helpful to show how composition influences the existence of these phases, and to determine the depth of oxygen incorporation. To this end, sputter depth profiling was performed to study composition as a function of depth in select as-deposited and annealed films. Operating conditions during sputtering included ( $2 \times 10^{-7}$  Torr) chamber pressure, with argon gas for etching. A sputter spot size of 2 mm<sup>2</sup> was made by sputtering material from the sample surface at approximately 0.54 Å/min, and the same 300  $\mu$ m monochromated Al K( $\alpha$ ) x-ray beam was used for analysis. The remainder of the sample (outside of the sputter area) was masked to avoid deposition of sputtered material from the surface elsewhere on the sample. Calibration of the sputter rate was performed using a silicon wafer (similar in atomic weight to the aluminum-based films) and determination of the step height by profilometry. Sputter rate was not adjusted for film roughness.

XPS depth profiling was performed on unannealed sample A8, and the resulting stoichiometry below 20 nm was stable at Al<sub>64</sub>Cu<sub>21.5</sub>Fe<sub>9.5</sub>O<sub>5</sub>. Samples A7 and A5 were quenched in liquid nitrogen after ampoule anneals of 1 and 10 hours, respectively. XPS depth profiling was used to compare the composition as a function of depth for the two annealing conditions, shown in Figure 13. Extensive oxygen incorporation was noted in the top 100 nm of both films and produced nearly stoichiometric Al<sub>2</sub>O<sub>3</sub> at the film surface, despite encapsulation in 500 mT argon gas. The composition profile was similar for both samples, but slight variations were noted. The 1 hour anneal produced a profile with aluminum concentration approximately constant beyond 50 nm. The 10 hour anneal at 450°C has produced a broadened profile with redistribution of aluminum from the 50 to 100 nm range toward the surface of the film. The aluminum concentration was determined to be constant only below 140 nm for the longer anneal. Aluminum enrichment at the surface of both films can be quantified by expressing the atomic percentage aluminum as a fraction of the combined percentages of all metallic components, at each depth, as shown in Figure 14. The degree of aluminum enrichment at the surface of both films is large compared to the same quantity in the unannealed film; however, the magnitude of enrichment is similar for both annealed samples regardless of additional annealing (given the experimental uncertainty of several atomic percent). In both cases, the percentage aluminum stabilized at approximately 70% in the bulk. The same quantity calculated for the unannealed film is also stable below 20 nm at 70%.

<sup>20</sup> C. J. Jenks, T. E. Bloomer, M. J. Kramer, T. A. Lograsso, D. W. Delaney, A. R. Ross, D. J. Sordet, M. F. Besser, P. A. Thiel, *Appl. Surf. Science* 180 (2001) 57.

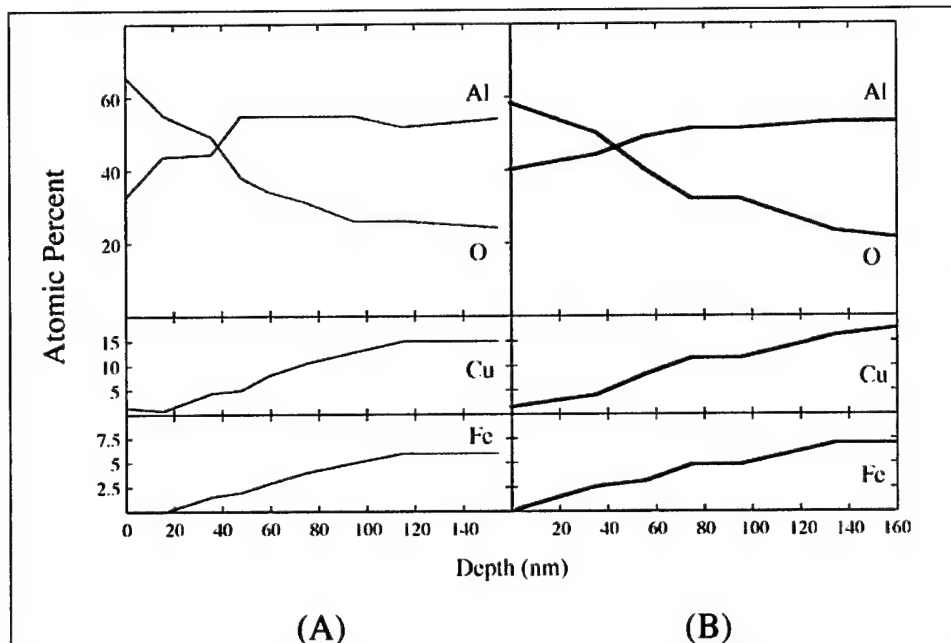


**Figure 13.** Composition as a function of depth as determined by XPS depth profiling for samples quenched in their ampoules in liquid nitrogen after 450°C anneals for 1 (A7) and 10 hours (A5), respectively.

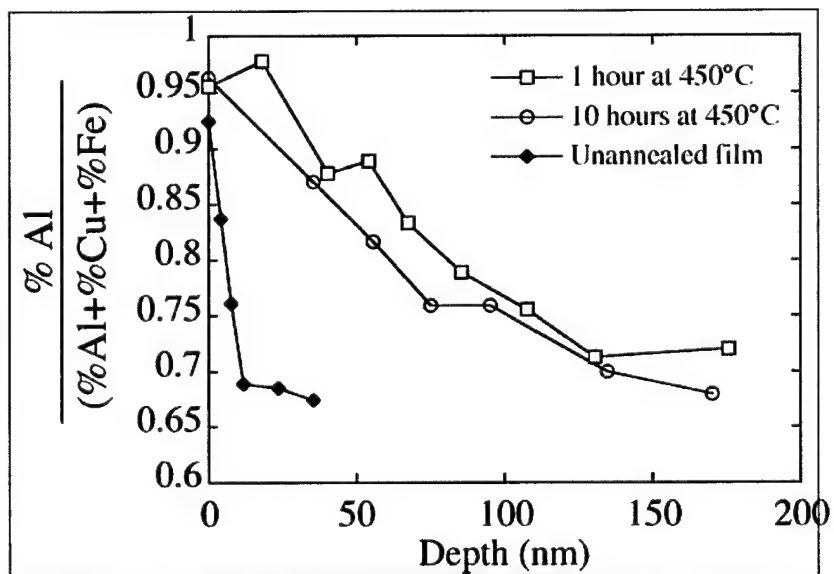


**Figure 14.** Atomic percent aluminum shown as a fraction of all metallic components (%Al + %Cu + %Fe) as a function of depth and annealing condition to emphasize surface enrichment of aluminum.

The same type of depth profiling was performed for sample A9, annealed at 500°C for 60 hours, and is shown in Figure 15. This depth profile illustrates the effect of prolonged annealing on oxygen incorporation and phase stability. Oxygen concentration increased above that observed in samples A5

and A7, above. After the prolonged anneal, oxygen concentration was only stable below approximately 250 nm. Due to the increased incorporation of oxygen in the film, it is clear that a passivation layer could not be forming under these annealing conditions.

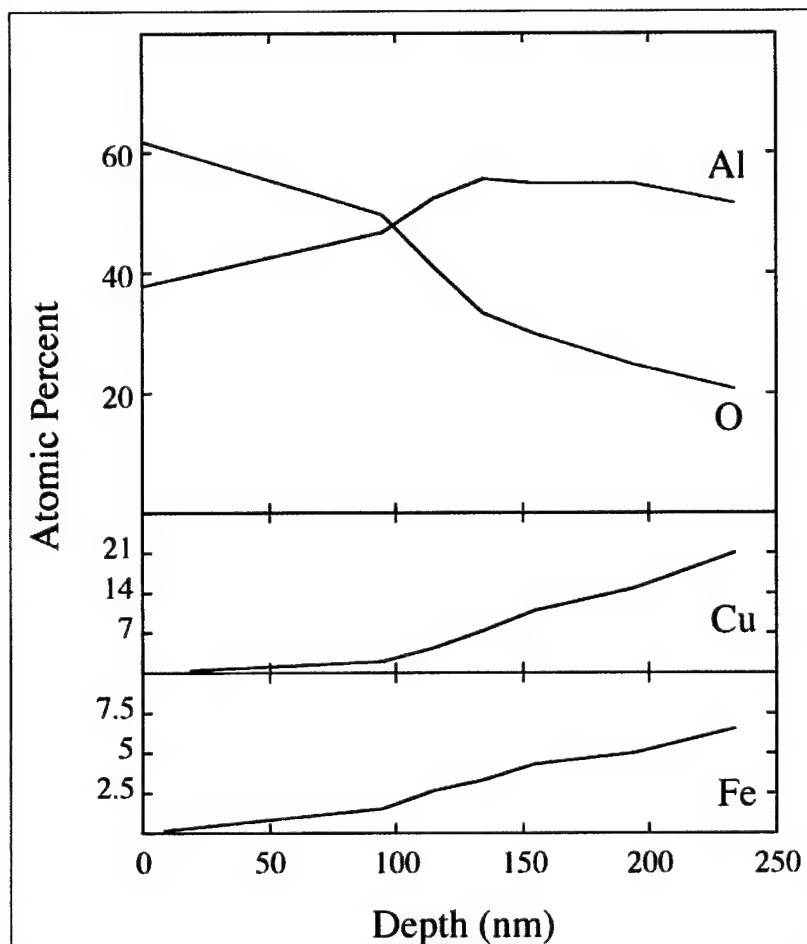


**Figure 15.** Composition as a function of depth as determined by XPS depth profiling for sample A9 quenched in its ampoule in liquid nitrogen after 500°C anneal for 60 hours.

**2.4 Microstructural Analysis** Grazing Incidence X-ray Scattering (GIXS) was performed on all films on BL 2-1 at the Stanford Synchrotron Radiation Laboratory (3 GeV, 100 mA to 60 mA at fill) at an incident energy of 10 keV ( $\lambda=1.240 \pm 0.001 \text{ \AA}$ ) or 8 keV ( $\lambda=1.550 \pm 0.001 \text{ \AA}$ ) in an asymmetric configuration. This configuration is briefly described as an incident beam fixed with respect to the film surface and lying in the same plane as the film normal and the  $2\theta$  measurement arc of diffraction. The angle formed between the surface of the film and the incident beam is small ( $0.02^\circ$  to  $4^\circ$ ) to probe a constant volume of the film and avoid substrate contribution. For certain groups of samples, raw counts are compared for all cases instead of a normalized comparison because samples were aligned at the same incident angle and probed in the same manner. A helium sample enclosure eliminated air scattering. In certain cases, depth profiling was also performed by scanning the sample at a variety of incident angles to take advantage of the finite penetration of the x-ray beam. In this manner, structural information is obtained as a function of depth.

The penetration depth of the incident beam was estimated based on the composition of the as-deposited films ( $\text{Al}_{64}\text{Cu}_{21.5}\text{Fe}_{9.5}\text{O}_5$ ), a density of  $3600 \text{ kg/m}^3$  for a similar composition,<sup>21</sup> and the LBL-CXRO program for attenuation length calculation.<sup>22,23</sup> The calculated penetration depth is shown as a function of incident angle in Figure 16 for both photon energies (8 keV and 10 keV). For all samples analyzed at  $\lambda=1.240 \text{ \AA}$ , a crystal analyzer on the detector arm limited divergence of the diffracted beams to less than 1 milliradian, which resulted in greatly enhanced peak resolution. For all scans performed with  $\lambda=1.550 \text{ \AA}$ , Soller slits were used to limit divergence of the diffracted beams to 1 milliradian. In all cases, an energy window on the detector limited the contribution of fluorescence to the diffracted intensity and a  $\text{LaB}_6$  standard was used for calibration.

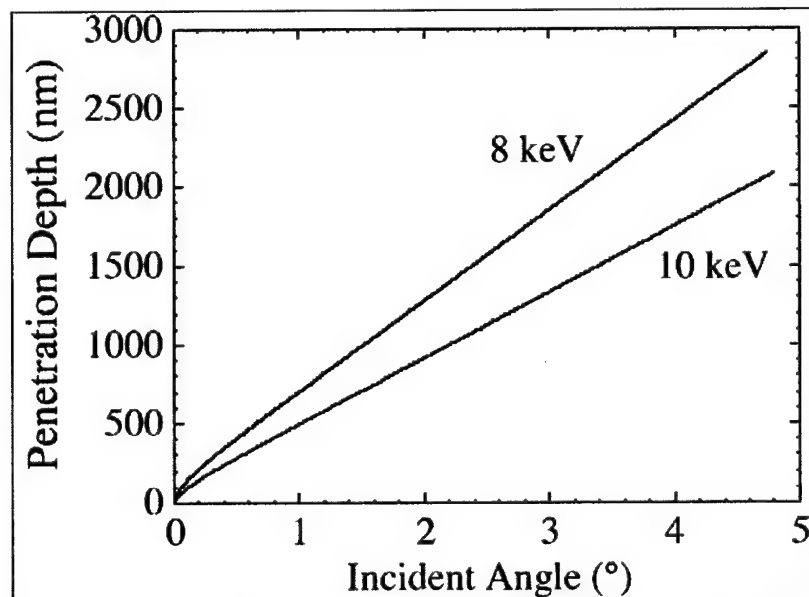


Figure 16. Calculated penetration depth of the synchrotron beam as a function of incident angle and photon energy.

## 2.5 Fluctuation Microscopy Results

The material that was most pertinent to this study was the oxide that formed on the quasicrystalline films fabricated by TA&T. There is evidence that much of the difference between alumina and the quasicrystalline oxide films (and their respective coefficients of friction) is due to the presence of medium range order in the quasicrystalline oxide. In order to study this difference, novel methods of fabricating plan view and cross section TEM foils of oxidized materials were used. These techniques utilized both focused ion beam milling and chemical etching from the backside. These initial studies focused on a high-resolution chemical analysis on cross-section samples using both an imaging filter and high resolution XEDS with a focused probe. This film is shown in Figure 17. The results of these studies suggested the following:

<sup>21</sup> J. M. Dubois, S. S. Kang, P. Archambault, B. Colletet, J. Mater. Res. 8, 1 (1993) 38.

<sup>22</sup> B.L. Henke, E.M. Gullikson, and J.C. Davis. X-ray interactions: photoabsorption, scattering, transmission, and reflection at  $E=50\text{-}30000 \text{ eV}$ ,  $Z=1\text{-}92$ , Atomic Data and Nuclear Data Tables Vol. 54 (no. 2), 181-342 (July 1993).

<sup>23</sup> E. Gullikson in Vacuum Ultraviolet Spectroscopy: Experimental Methods in the Physical Sciences, Academic Press, San Diego (1998) 257.

- Regions 1-6 contain oxygen in significant proportions
- There is less than  $\approx 5$  atomic % in regions 7-10
- Cu and Fe appear to be absent from the oxide - more work is needed to verify this observation

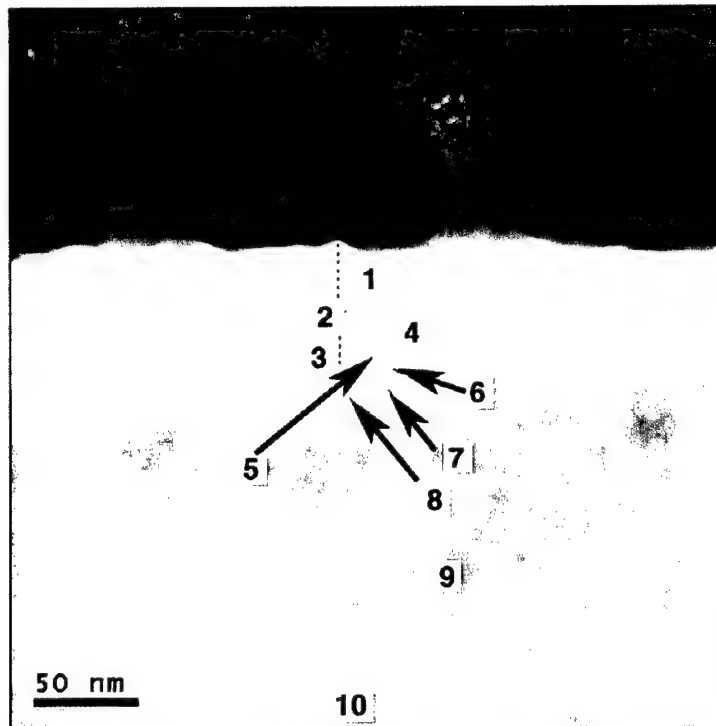


**Figure 17.** A TEM image of the positions that XEDS analysis was performed and the XEDS data shown in figure 8.

The XEDS data shown in Figure 24 show the chemistry of 10 nm regions of the cross section sample (made with a Focused Ion Beam compliments of Wright Patterson AFB). The peaks that are visible at position 1 have a small peak corresponding to Au. This is to be expected because the sample was coated with Au to protect the top surface during the FIB process. There will always be a small contribution from material that is within several hundred nm because of multiple scattering of electrons and re-absorption of x-rays. The magnitude and the ratio of the L lines to the K lines in the heavier elements are the keys to interpreting the data. The Al peak is clearly visible in all of the data points (of course there is only one peak expected from Al). The presence of Cu-L peaks in the spectra at points 4 and 5 are artifacts from re-scattering from the very close metal substrate. This is obvious because the other Cu peaks are very small or absent. When the data is collected from the substrate (points 6 through 10, both copper peaks are present in the right ratio. The conclusion is reached that the oxide is primarily (within  $\approx 5$  atomic percent) alumina. This result is not surprising because alumina has a much higher heat of formation than any of the other oxides and more readily combines with oxygen at the surface. Hence, the other oxides, which may form from the other elements in the metal film, have a lower thermodynamic driving force and if present, would be in very low concentrations.

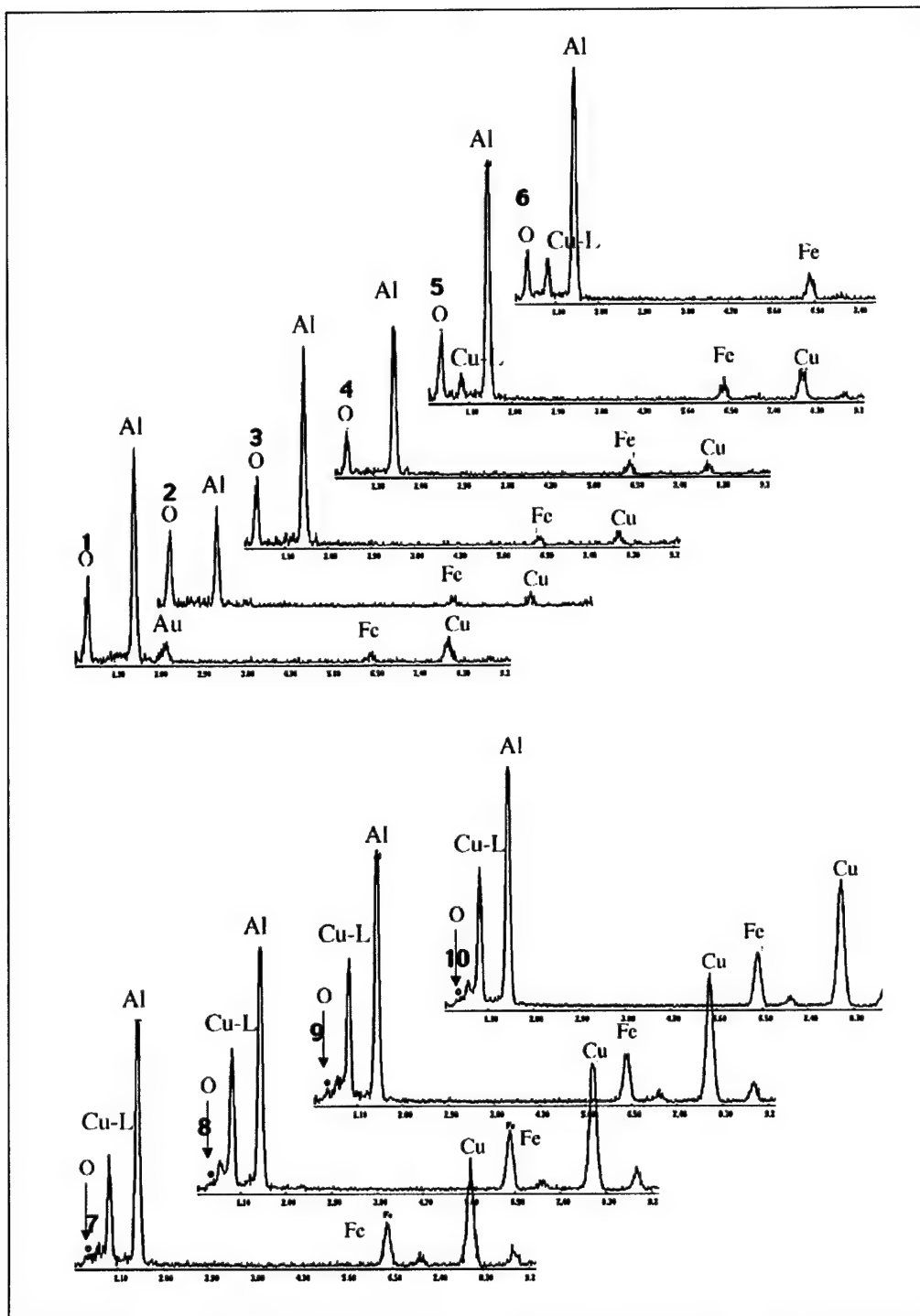


**Figure 18.** XEDS data from each labeled point in Figure 17.

Fluctuation microscopy analysis was used in this study to determine the degree and type of order contained in oxides formed on AlCuFe coatings and oxidized aluminum. The goal was to compare thermally grown alumina formed on oxidized aluminum to the thermally grown oxides of the



quasicrystalline (and approximant) films. A new method for fabricating samples was used so that very thin ( $\sim 200$  Å) flat films with a great deal of electron transparent area (hundreds of microns) could be studied. Discs of Al foil were oxidized in a furnace at  $600^{\circ}\text{C}$  for 20-24 hours. The diffraction pattern and fluctuation microscopy results from these samples are shown in Figures 19 and 20, respectively. These results will be compared to those from AlCuFe samples below. AlCuFe sputtered film from run 1062 was supplied (as-deposited) by Technology Assessment and Transfer on Si wafers and was also subjected to the same oxidation conditions. Small ( $<1\text{ cm}^2$ ) pieces were used to avoid cracking the films when they went through the phase transformation. Discs were ultrasonically machined from these samples. In both cases, the discs were polished from the backside (the oxide on the side to be etched must be removed before etching) and etched with a buffered HF solution to perforation while protecting the oxidized surface with wax. Because HF etches both metals and Si at a far higher rate than alumina, all of the metal was etched away, leaving only the oxide.

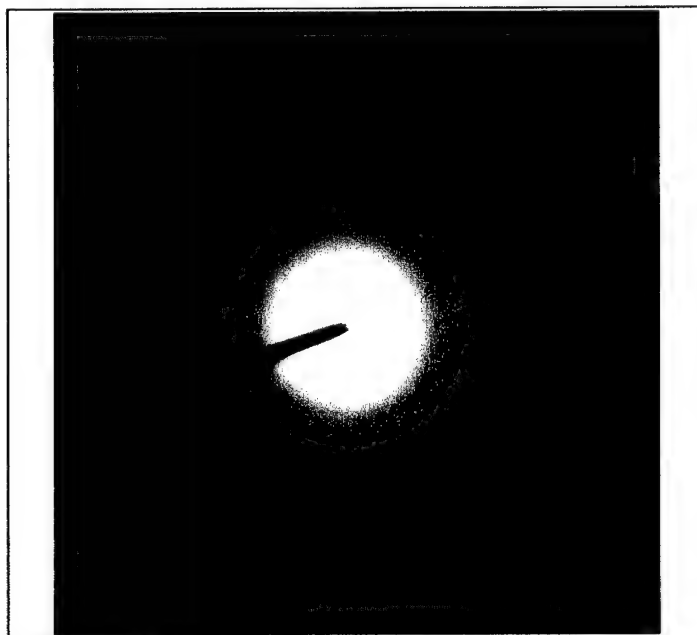


**Figure 19. Diffraction Pattern from the oxide formed on an Al foil annealed for 24 Hours at  $600^{\circ}\text{C}$ .**

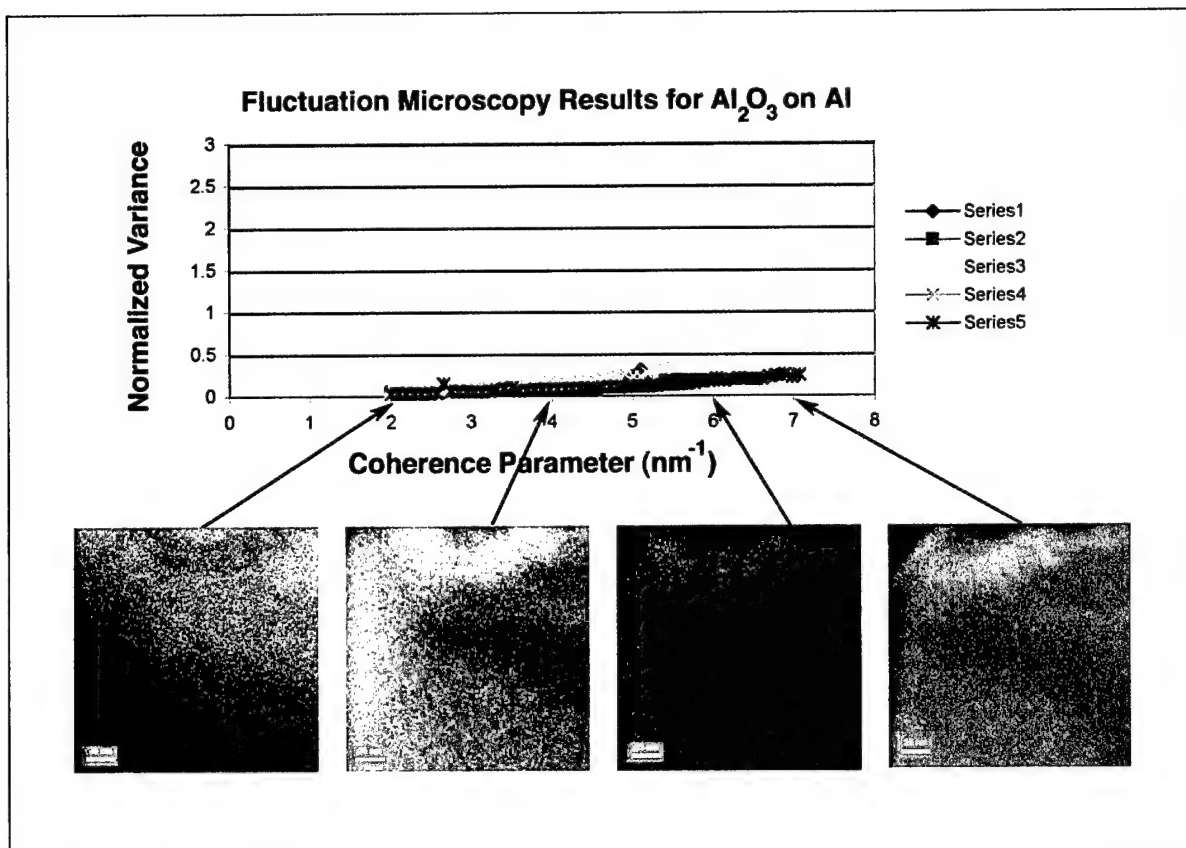


**Figure 20. Fluctuation microscopy results and typical images from oxide of Al**

The data presented in this work were taken from samples with the AlCuFe ternary composition that has been reported to have extraordinary tribological properties. The diffraction pattern for this film is shown in Figure 19. Here the diffraction pattern appears to contain polycrystalline material in an amorphous matrix. The fluctuation microscopy results are consistent with the diffraction pattern. Figure 20 shows the large peak centered at  $8 \text{ nm}^{-1}$ . The images show a wide range of contrasts as a function of tilt angle and there are also regions of the film that appear to be crystalline. In comparison to similar studies on aluminum presented in Figures 14 and 15 which showed little variance with coherence parameter, the results from the AlCuFe films present clear evidence that there is medium range order. If it were polycrystalline only, then the peak would be much narrower.

To check the robustness of these results, the cross section (FIBed) sample in Figure 17 was examined. Fluctuation microscopy was not performed on this sample because the area was a long thin strip of oxide, and there is currently no methodology capable of analyzing this kind of sample. Instead, the sample was tilted, and dark field images were collected at the same coherence parameters as illustrated in Figure 20. Those results are shown in Figure 23. The data show that the oxide is partially crystalline and has a component of medium range order as well. This sample had been oxidized by TA&T for 96 hours in air at  $500^\circ\text{C}$  (TA&T number 1062). The sample that produced the results of Figures 21 and 22 was also from TA&T run number 1062, but the sample from Figures 21 and 22 was annealed at  $600^\circ\text{C}$  for 24 hours.

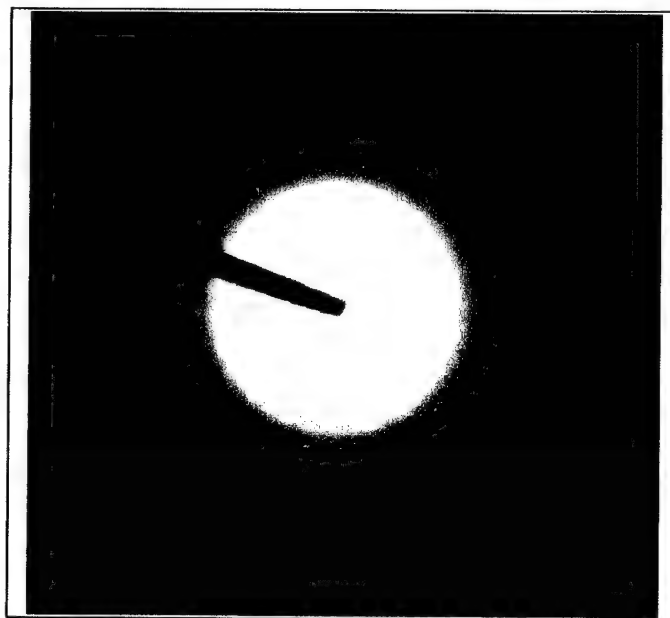


Figure 21: Diffraction Pattern from Oxide of Al-Cu-Fe annealed for 24 Hours at 600C

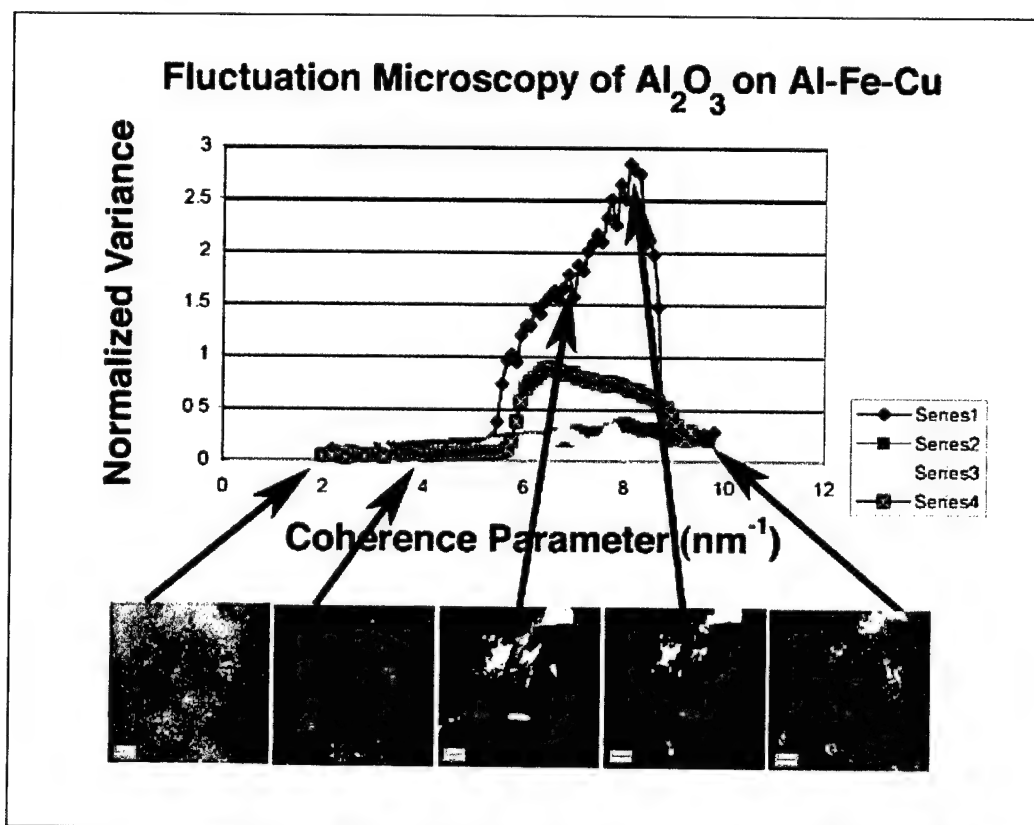
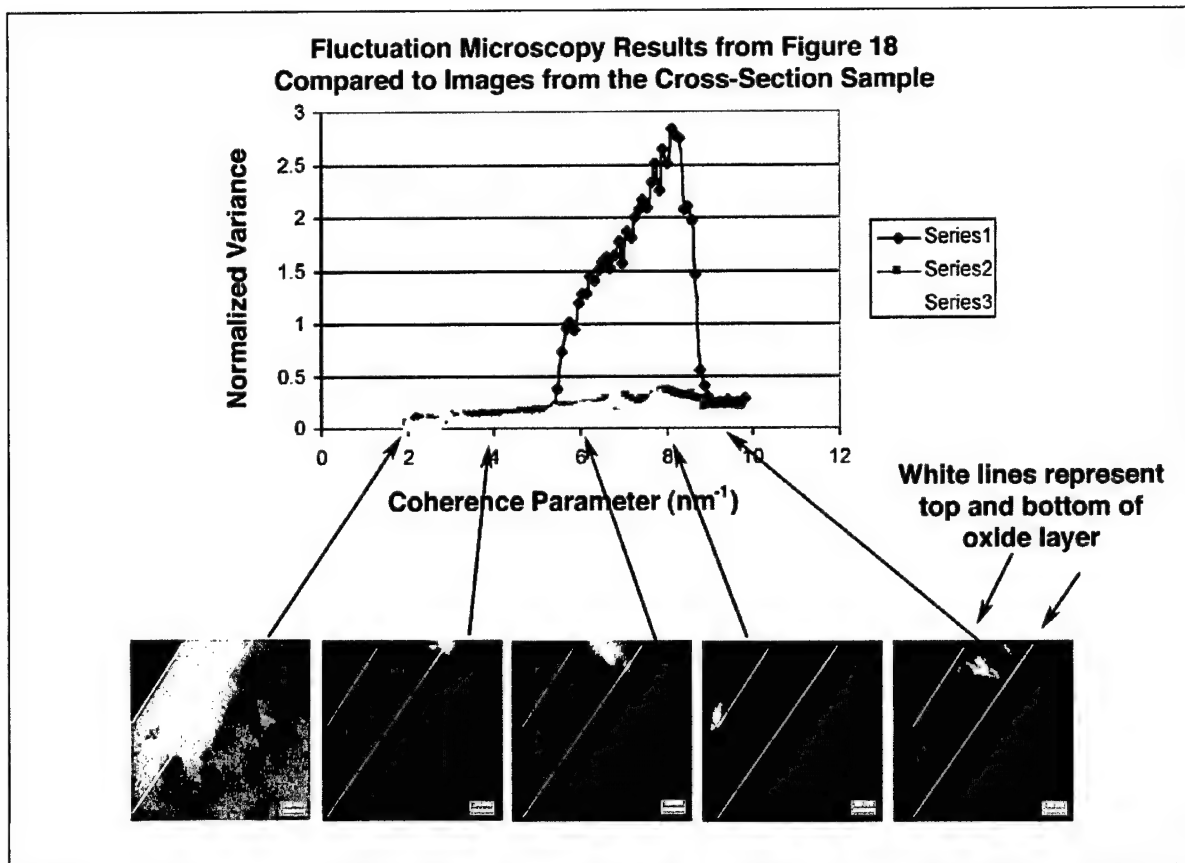


Figure 22. Fluctuation microscopy results and typical images from oxide of Al-Cu-Fe



**Figure 23.** Comparison of tilted images from the cross-sectioned sample (run number 1062 that TAT annealed) to sample annealed at Michigan (also run number 1062)

## 2.6 Summary of Microstructural Analysis

R-phase films have been formed by deposition of precursor films via RF sputtering and *ex situ* annealing below 600°C and at 850°C. The R-phase phase is formed at 450°C and above, below the previously reported value of 475°C. A gradual transition was observed in the diffraction pattern from the structure of the precursor film to the R-phase in a film annealed for 1 hour at 450°C, suggesting a grain growth process, rather than a phase transformation. A  $\beta$  phase and  $\lambda$  phase were also present in conjunction with the R-phase at various points during annealing. Aluminum enrichment at the surface of the film, as well as preferential oxidation of aluminum, were found to cause formation of aluminum-deficient  $\beta$  phase. Aluminum-rich  $\lambda$  impurities also formed due to localized compositional variations in some regions. Both impurity phases were absent in anneals of 10 hours at 450°C and in other anneals at higher temperatures. Cooling rates of 2.9°C/sec and 1.1°C/sec were investigated for samples in quartz ampoules cooled from their anneal temperatures, and peak breadth was found not to be dependent on the cooling rate within this range. Peak breadth was also found to be not dependent on anneal time or temperature, once the R-phase was fully formed. In addition, extended annealing for 60 hours at 500°C showed that despite an increased level of oxygen incorporation, no oxide phases or secondary impurities formed. The long-term oxidation phase stability and resistance to oxidation is demonstrated. This was shown in contrast to an anneal performed at 850°C which showed several impurity phases, in addition to the quasicrystalline structure.

The work presented here has accurately determined the processing window of the annealing treatment necessary to produce stable and single-phase rhombohedral approximant coatings. While anneals at 450°C will form the R-phase over extended periods of time, minor impurity phases are likely. Instead, annealing treatments at 500 to 550°C for 1 hour with a quench rate of 1.1°C-sec<sup>-1</sup> or greater are most effective in forming the R-phase without extra oxygen incorporation.

## 2.7 Corrosion Resistance of AlCuFe, AlCuFeCr and AlCoFeCr alloys

In completion of other work, funded by the Air Force Research Laboratory, TA&T has identified potentially useful corrosion resistant properties of Al-Transition Metal (Al-TM) quasicrystalline coatings. Anecdotal accounts had been made previously by subcontractors at the University of Michigan about the extreme degree of resistance of quasicrystalline precursor films to acid attack during chemical thinning of transmission electron microscopy samples. The corrosion resistance of these alloy films was tested using potentiodynamic scans (PDS) and electrochemical impedance spectroscopic scans performed on quasicrystalline alloy films deposited at TA&T. The results of these comparative tests are shown in Figures 24 and 25.

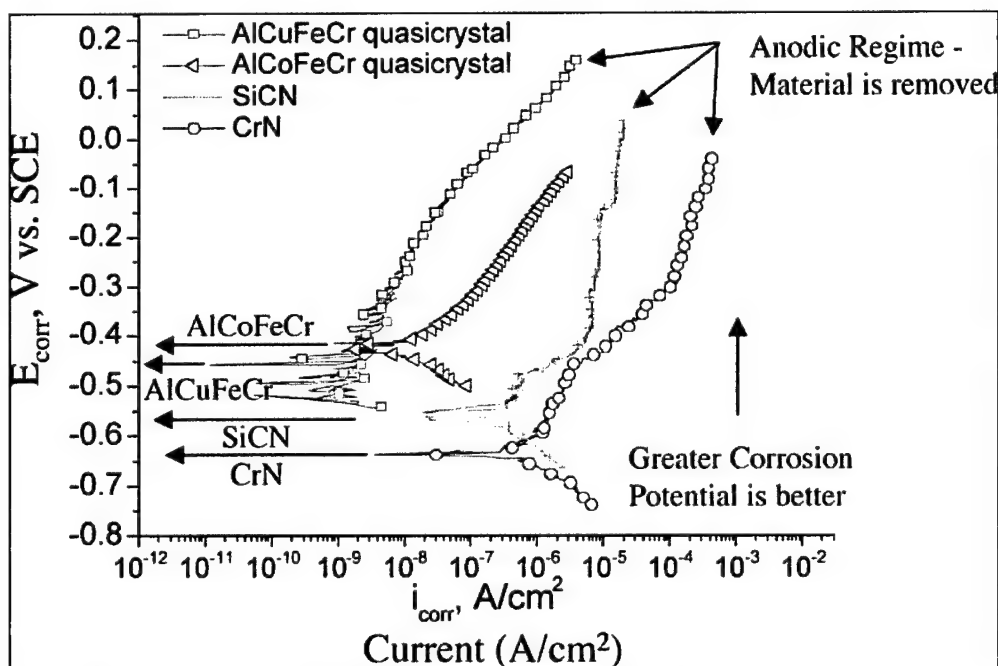
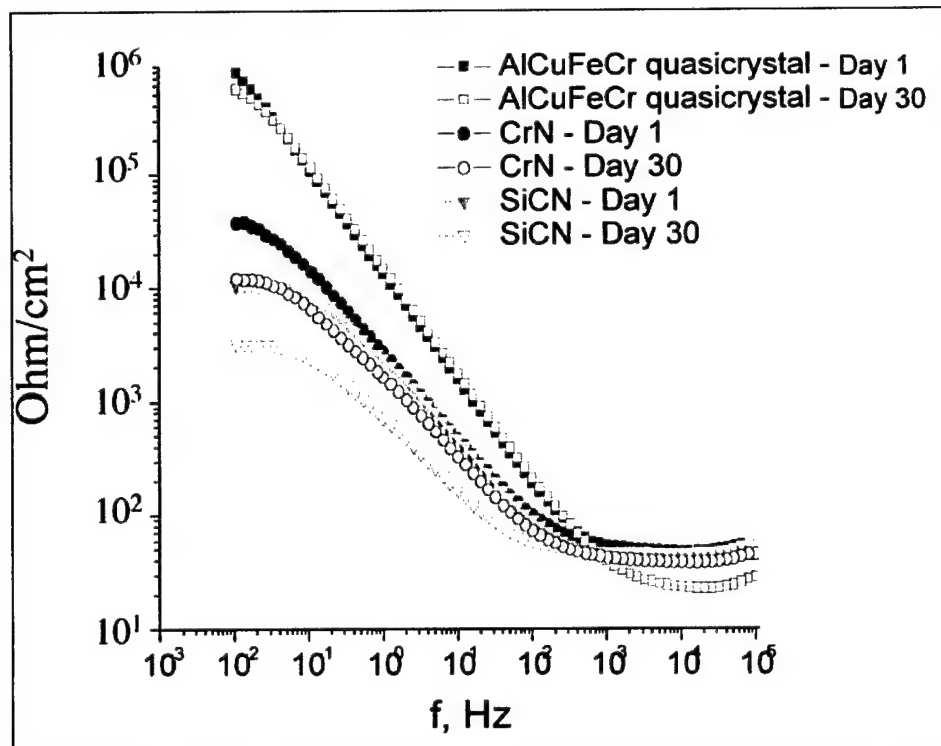


Figure 24. PDS results from AlCuFeCr and AlCoFeCr as-deposited quasicrystalline films against other common coating materials. The plateau corresponds to the corrosion potential of the material.



**Figure 25.** Results of EIS measurements performed on an AlCuFeCr as-deposited quasicrystalline film in Harrison's solution compared against the results from similar tests performed on other corrosion resistant coatings. The overlay of the AlCuFeCr lines shows that little corrosion has occurred.

TA&T, Inc. has also contacted Dr. Derek Demaree of the Army Research Laboratory to explore potential uses for these Al-TM coatings as corrosion resistant coatings for use in Army applications. TA&T is investigating a possible Cooperative Research and Development Agreement (CRADA) for this technology with the Army Research Laboratory.

The reasons for the exceptional corrosion resistance of these AlCoFeCr alloys was a recent investigation of a Phase I Small Business Innovative Research contract from the U.S. Air Force. Fundamental work, which will be pursued under a Phase II contract, is still needed to identify the morphological, structural, and compositional basis for the corrosion resistance of these films. In addition, resistance to mechanical damage will be explored.

### 3. STEAM ENGINE TRIBOLOGY

Four subsections comprise this section:

- Overview and rationale,
- Tribometer modifications and description,
- Tribometer performance characteristics,
- Friction and wear measurements on steam engine tribo-materials.

**3.1 Overview and Rationale** As presented in Section 1, a fifth objective of this research was to explore low-friction, low-wear thin film coating systems for use in steam engine environments with steam temperatures to 600°C. Friction and wear testing of thin films under these conditions presented several major technical challenges. Few high temperature tribometers exist anywhere in the world, and even fewer operate under a steam environment. TA&T modified for steam environment testing a precision tribometer originally developed by Dr. Michael Gardos for high temperature tribological measurements. It consists of a rotating sample and rub block, and allows measurement of the normal force, the frictional force, the temperature, and the in situ wear rate in real time. Prior to the work reported on here, TA&T had already modified this tribometer to perform real time studies of the effects of corrosion on friction and wear in a salt spray environment to study the corrosion inhibiting properties of quasicrystalline and other thin film systems such as Argonne's Near Frictionless Carbon.

The Gardos Tester offers several benefits over tribological testing with the Hohman system. The most important of these is that the samples for the Gardos tester are simple rods, rather than the Timkin cup configuration required by the Hohman system. Machining of the sleeve samples from the myriad of substrates proposed here would have been prohibitively expensive.

Furthermore, the curved nature of the sleeve makes coating deposition more difficult. The energetic of the deposition system also change due to the curved substrate. Target-to-substrate distance is a major factor in determining the energy of an incoming adatom as it reaches the sample surface. Adatoms with high energy have a greater degree of mobility on the surface, and different equilibrium or non-equilibrium crystal structures may form at varying adatom energies. The curved configuration of the Hohman tester means that any coating deposited on this substrate could have potentially different crystal structures on different parts of the same sample. Impingement angle of adatoms on the substrate is also different at various points on the sample. Overall, these factors point to the likelihood of inconsistencies in crystal structure, porosity, and morphology. The rod sample configuration of the Gardos tester is simple to coat in the Sloan 1800 magnetron sputtering system used throughout this effort, and does not suffer from the aforementioned problems with the Hohman system. This is the basic, unmodified Gardos Tester.

**3.2 Tribometer Modifications and Description** Early in this effort, Dr. Michael Gardos, COTR for this project, indicated his desire that tribometer system (hereafter referred to as "Gardos Tester") developed by him be modified for the purposes of testing at elevated temperature and in steam environment, rather than the Hohman tribometer originally proposed for this work. This proved to be a wise decision since modifications of the Gardos Tester were easier to implement than those proposed for the Hohman.

A schematic overview of the basic system and relevant components is shown in Figure 26. Each experiment used two 3/8" diameter rods: one rod was about 3" long (referred to as the "rotating rod sample" in Figure 26); the other rod was about 1 1/2" long (referred to as the "rub block" in Figure 26). Details of the material couple are shown in Figure 27.

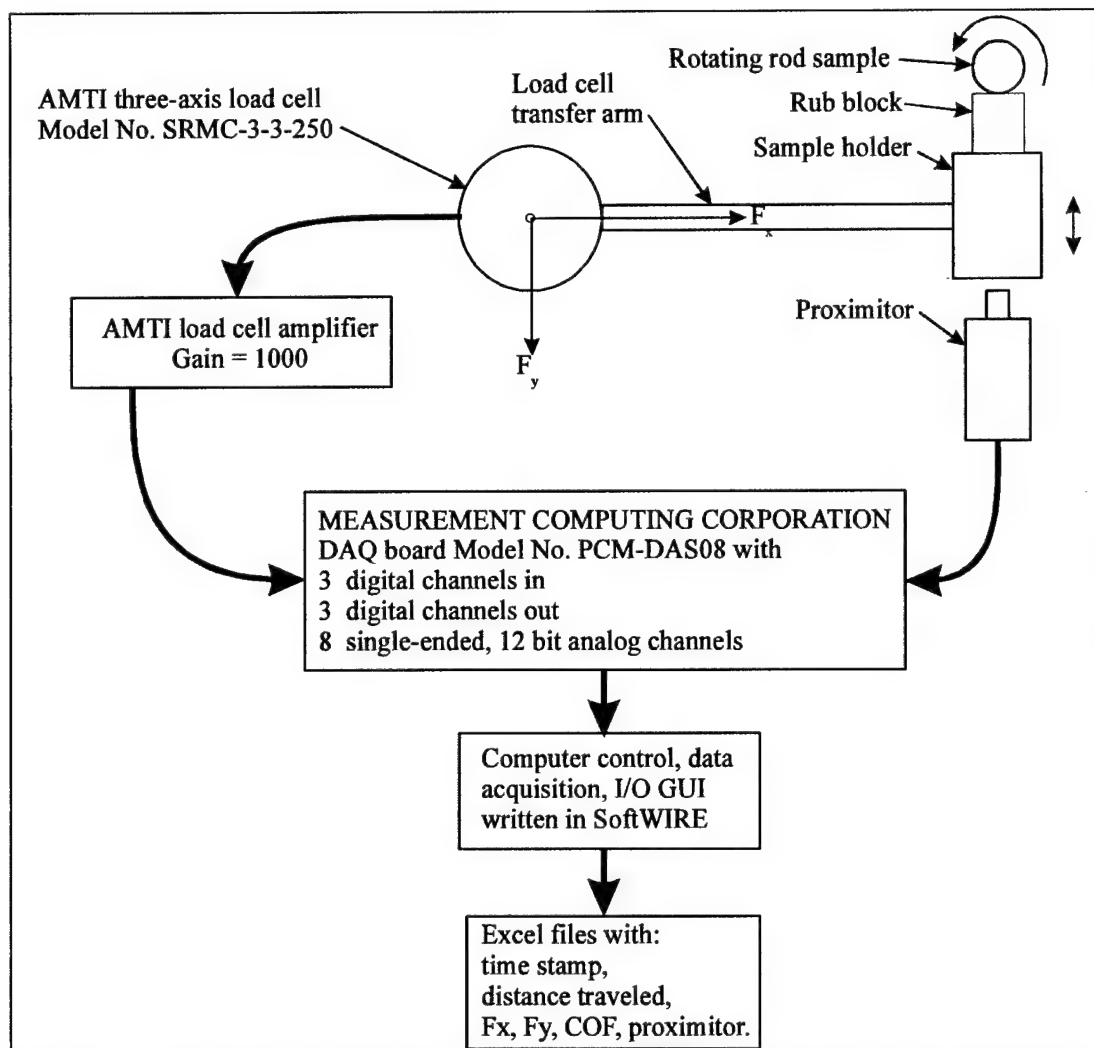


**Figure 26. Overview of the Gardos Tester and components. A normal force is applied to the rub block during rotation of the rod sample. A three-axis load cell measures the frictional force between the rotating sample and rub block, and SoftWIRE™ software is used to calculate the frictional force in the interface at preset intervals.**



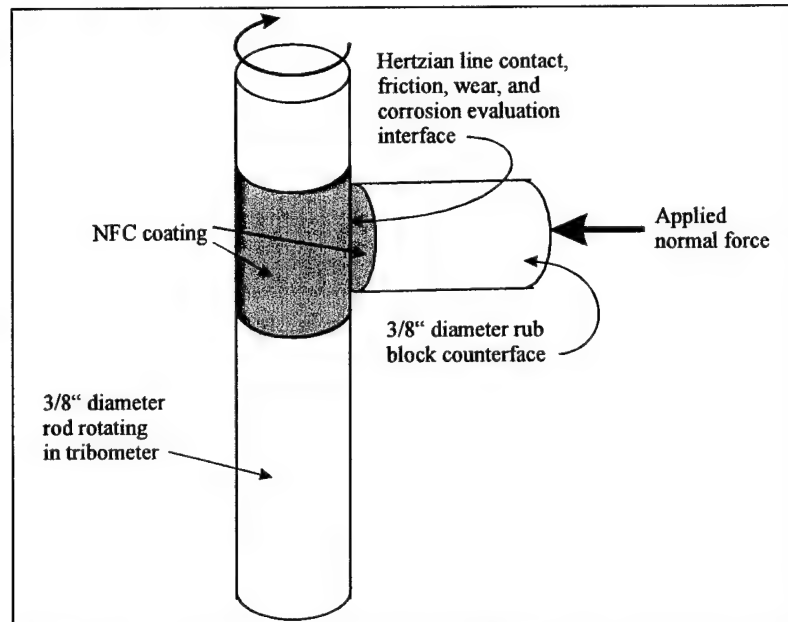


**Figure 27.** Schematic of the Gardos Tester wear interface. The vertical rod rotates, creating a Hertzian line contact with the rub block with an applied normal force.

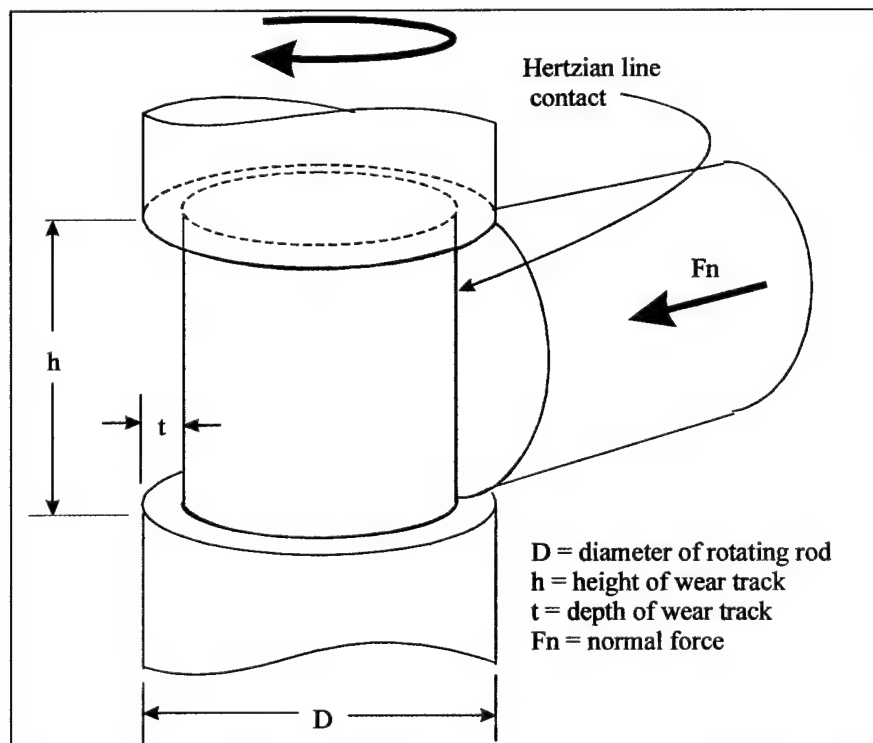


**Figure 28.** Schematic of wear volume

Using data generated by the Proximator<sup>24</sup> shown in Figure 26 it is possible to compute a wear coefficient. The geometry for this calculation is shown in Figure 28. From Archard's equation, the wear rate,  $W$ , is given by the ratio of the wear volume,  $V$ , and the sliding distance,  $L$ , as

$$W = V/L \quad (1).$$

The explicit form this takes depends on the wear mechanism.<sup>25</sup> For all wear mechanisms, the general form is

$$W \propto K' F_n \quad (2)$$

Where  $K'$  is the wear coefficient. Replacing the proportionality with an equality, a new wear coefficient can be defined that is independent of the wear model but does account for the dependence on the applied force,

$$K = (V/L) (1/F_n) (m^2/Nt) \quad (3).$$

Figure 28 shows that  $V \approx \pi D h t$  since  $t \ll D$ ,  $h$ . All proximator data acquired during the course of this research could be very accurately expressed as  $t = \alpha L$  where  $\alpha$  is the slope of the proximeter data. In other words, the wear increases linearly with distance (or time). Putting all of this together,

$$K = (\pi D h \alpha L)/(L F_n) = (\pi D h \alpha)/F_n \quad (4).$$

For the experimental configuration being used here,  $h = D$  since the rotating rod and the rub block counterface are the same diameter so that equation (4) becomes

$$K = \pi D^2 \alpha / F_n \quad (5).$$

Equation 5 was used to calculate an effective wear coefficient.

Beginning with the basic Gardos Tester, six modifications were performed by TA&T to enable use of the Gardos Tester in a steam environment. These were:

1. A new Leeson Speedmaster Adjustable Speed Motor Controller was purchased to maintain constant speed control. After installation of the controller and replacement of bearings, the system is now capable of operating between 60 rpm and 800 PRM.
2. Various heating methods were explored. A system utilizing a series of focused, 500 Watt EHA projector bulbs was designed and built. A similar system has been used elsewhere to achieve similar temperatures in the 600°C range.<sup>26,27,28</sup>

<sup>24</sup> "Proximator" is a trade name of Bently-Nevada.

<sup>25</sup> Bhushan, B. and Gupta, B. K., Handbook of Tribology: Materials, Coatings, and Surface Treatments, (New York, McGraw-Hill: 1991), Section 2.

<sup>26</sup> B. L. French and J. C. Bilello, J. Appl. Phys. 94 (2) (2003) 224.

<sup>27</sup> B. L. French and J. C. Bilello, Mat. Res. Soc. Symp. Proc. 695 (2002) 385.

<sup>28</sup> B. L. French and J. C. Bilello, Thin Solid Films, In press (2003).

3. SoftWIRE™ was used to program a software code to record, in real time, the coefficient of friction and wear rate observed in the interface between the rub block and rotating rod. The Visual Basic code flowchart for this complex code is shown below in Figure 29.

4. An environmental chamber was fabricated from 316 stainless steel to house the focused lamp system and provide a closed atmosphere for testing of these parts. This material is known to resist corrosion, even in natural salt water solutions. In addition, a moisture shield was fabricated to protect the collet (which holds the rotating rod) and bearings from exposure to high temperature steam. Several photos of these modifications are shown below in Figures 30, 31, and 32.

5. The system was successfully tested for its capability to reach the proposed test temperature of 600°C. The length of time required to reach this temperature ( $\approx 30$  minutes) may be prohibitively long for the purposes of these tests, and alternative heating methods are also being explored. Additionally, the heating elements experienced unacceptable thermal stresses, and would probably not survive lifetime testing of the films.

6. Steam was injected into the chamber from a Sussman 3 kilowatt steam boiler operated continuously throughout each test run.

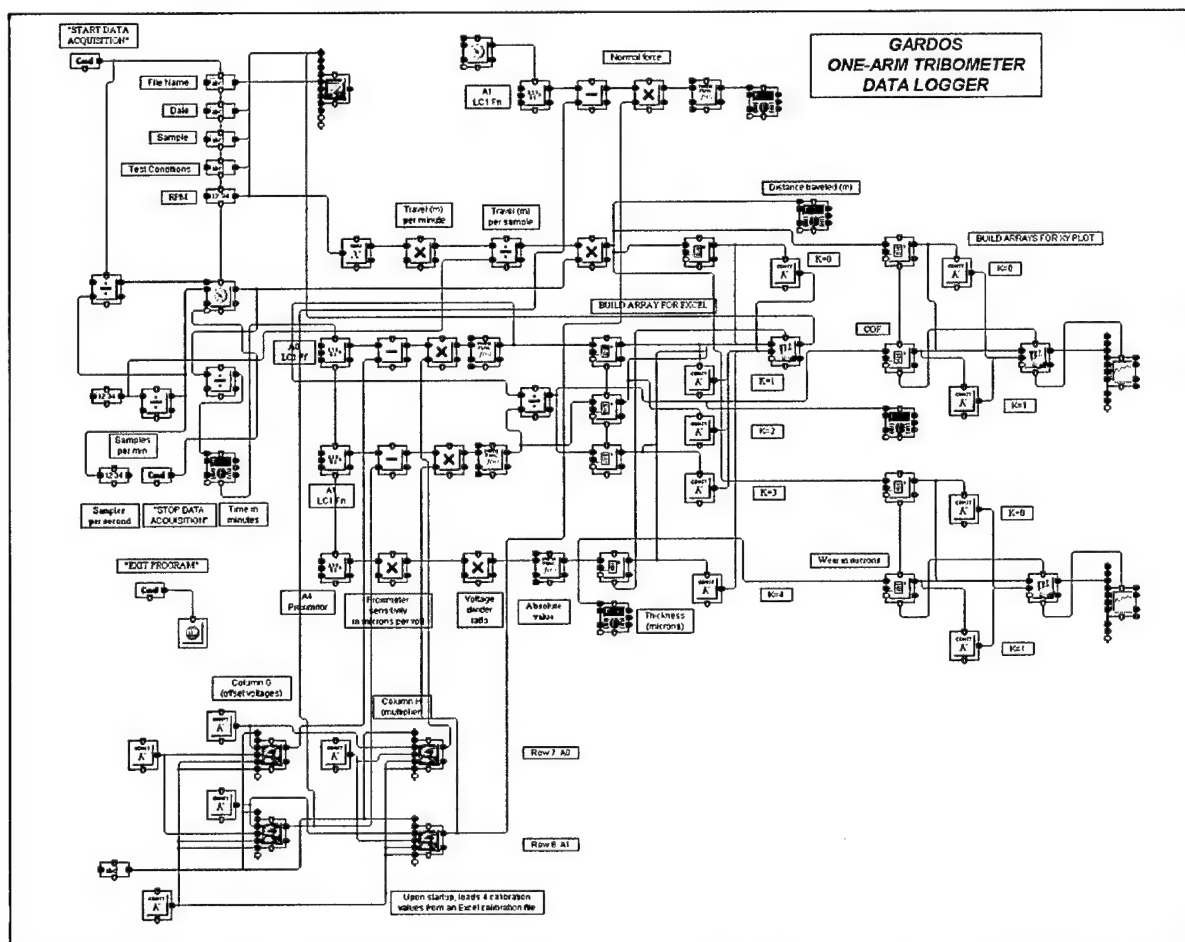
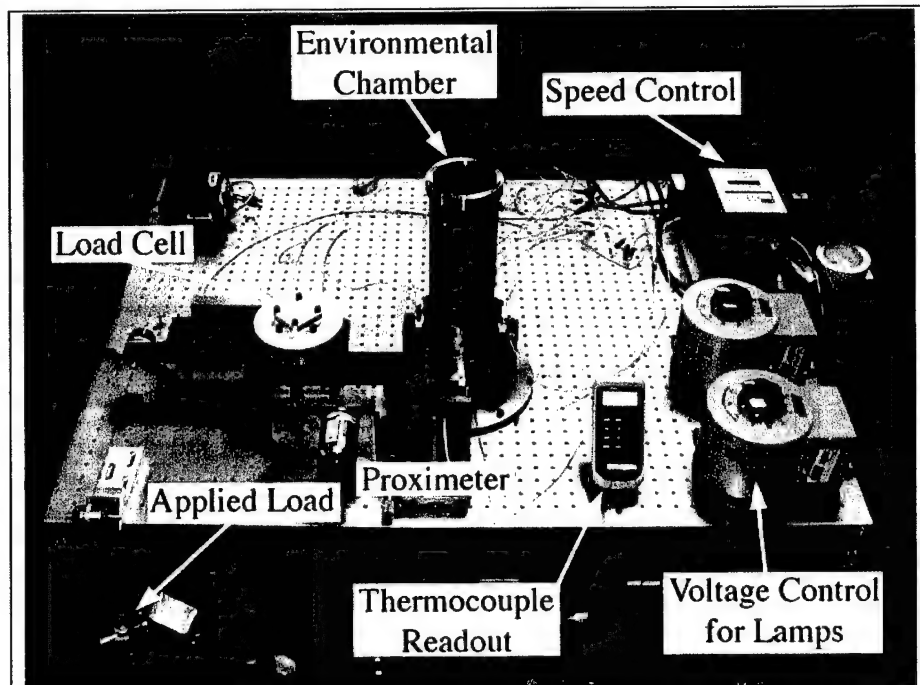
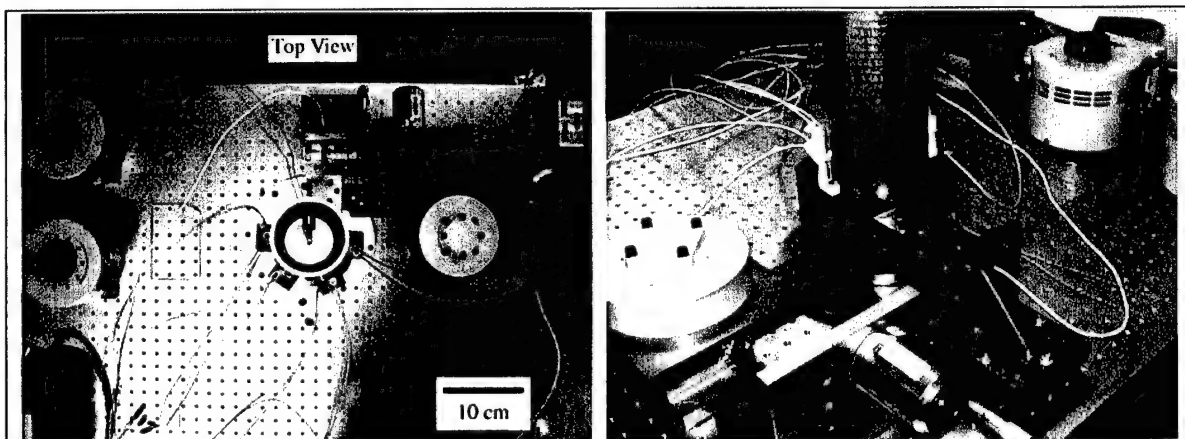


Figure 29. SoftWIRE control and measurement wire diagram for the Gardos Tester



**Figure 30. Hughes Tribological Tester with Modifications performed by TA&T. Modifications include a new motor speed control system, environmental chamber, and heat lamps and power supplies to heat the sample to 600°C.**



**Figure 31. (left) Top view of the environmental chamber with its cover removed. The tribological test pieces are visible in the center of the cylinder. (right) Side view of the tribological test system with the environmental chamber in place.**

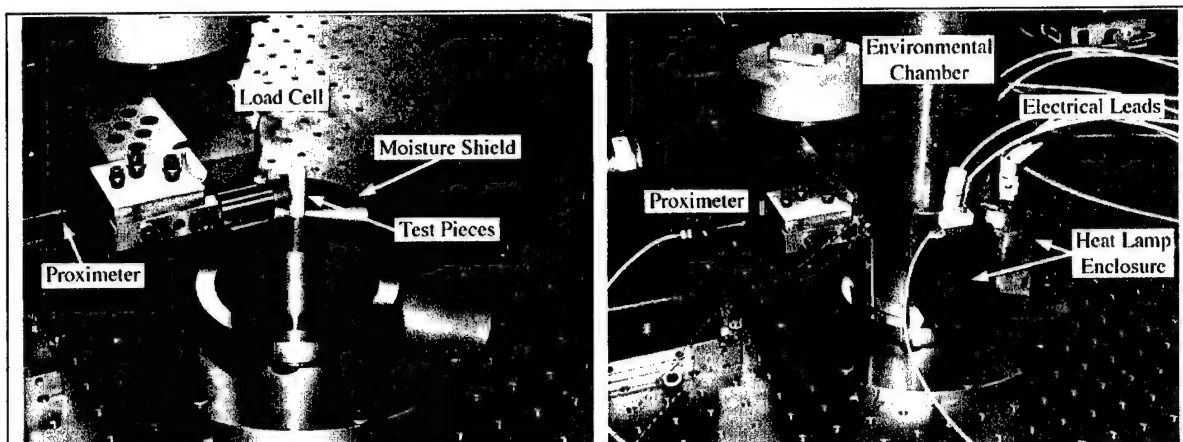


**Figure 32.** (left) Moisture shield that covers the collet during high temperature operation and exposure to steam. (right) Similar view of the environmental chamber with the enclosure in place.

### 3.3 Tribometer Performance Characteristics

Three external phenomena affected the data:

1. ambient air flow over the measurement arm and load cell,
2. sampling rate of the data acquisition hardware and sample eccentricity,
3. ambient temperature of the load cell.

**3.3.1 Ambient air flow** Changes in ambient air flowing across the test arm and/or load cell introduces a real force on the test arm that is sensed by the load cell and recorded as a real change in the normal or frictional forces. Figures 33a, b, c show the considerable size of this effect. Prior to this test, the arm had been calibrated to read 3.5 lbF and during the test the sample was not rotating. Therefore, the applied normal force should have been recorded as 3.5, and both the drag force and COF should have been recorded as 0. Clearly, changes in the ambient air flow had a dramatic effect. This was eliminated by enclosing the arm and load cell in a box.

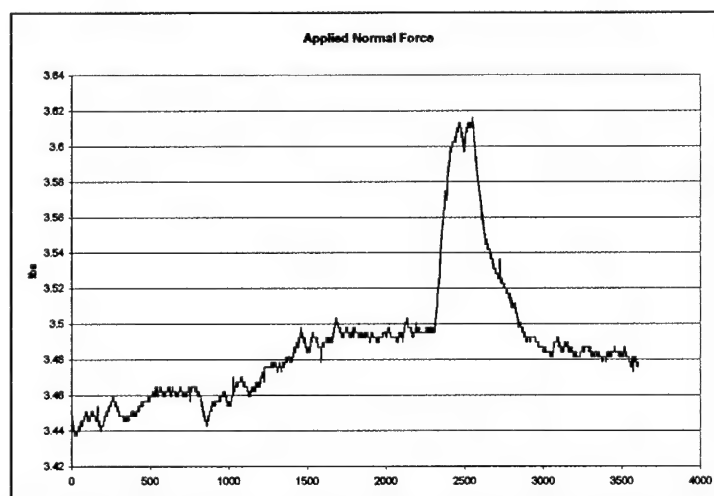


**Figure 33a.** Effect of changes in ambient air flow over the test arm and load cell

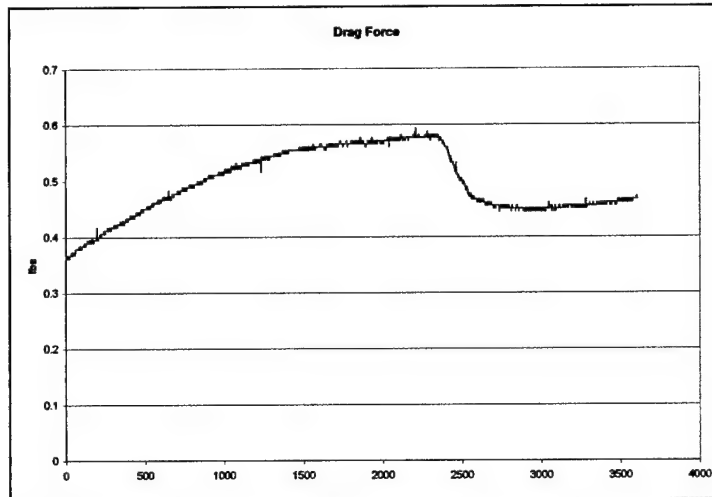


**Figure 33b. Effect of changes in ambient air flow over the test arm and load cell**

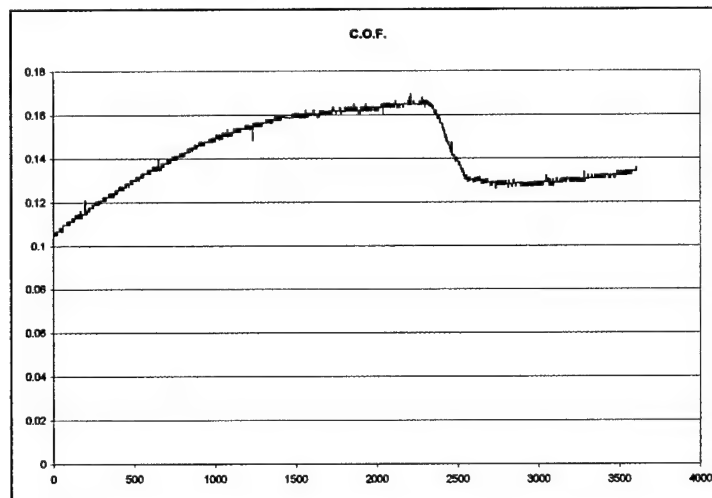


**Figure 33c. Effect of changes in ambient air flow over the test arm and load cell**

Figure 33 also exposes the 1 bit uncertainty that results from the limited resolution of a 12-bit A/D data acquisition board. This limitation also applies to the proximator accuracy reducing it to  $\pm 1.3 \mu\text{m}$  at best.

**3.3.2 Sampling rate** A second experimental effect resulted from a connection between either out-of-round or eccentrically mounted sample rods and the finite data sampling rate. Both would be expected to produce oscillatory data. Oscillation of proximator data obvious result and an extreme example of this is shown in Figure 34. Oscillations in the normal force are also observed and are a result of the inertia of the arm and rub block holder. As the axis of the rod moves toward the rub block, the normal force increases, and conversely as the axis moves away from the rub block. The effect is dynamic – the rod must be rotating – and if the arm and sample holder had zero mass, there would be no observed effect. If the true coefficient of friction is constant, then since the drag (frictional) force is proportional to the normal force, the measured frictional force and apparent COF also oscillates.

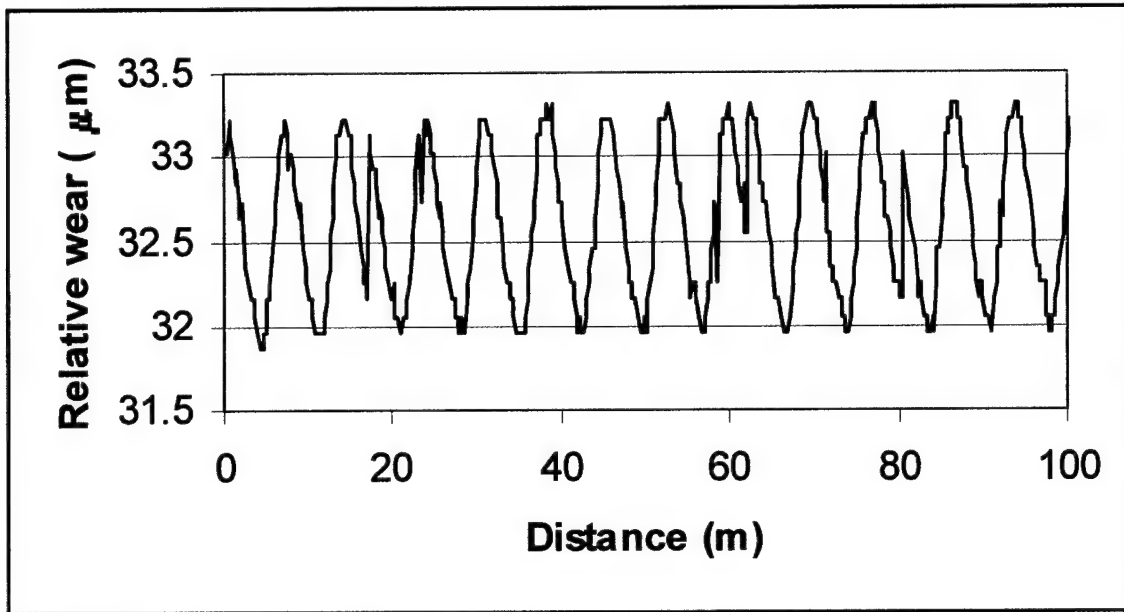


**Figure 34. Example of oscillatory proximator response resulting from an eccentrically shaped sample rod.**

In the experimental configuration, the rod was rotating at 200 – 240 rpm. At 240 rpm, for example, the period of oscillation would be 250 ms or 0.03 m, but Figure 34 shows that the observed period is in the range of 5 – 7 meters. This difference is due to the relatively low sampling rate of the computer data acquisition board. This rate was set to one sample per second – close to the limit of the board's capability. Figure 35 is a simulation of an eccentrically mounted rod rotating at 241 rpm and at 240 rpm. The eccentricity is simulated by a sinusoidal function with a period corresponding to the rotation rate, and the effect of sampling is simulated by sampling this function once per second. The effect of discrete sampling is dramatic. Since the actual experimental rotation rate of the rod cannot be maintained with accuracy sufficient to eliminate this artifact, most of the raw data exhibits this phenomenon. In fact, much of the data reveals that the motor rpm drifts during the course of a measurement which may last several hours. If the sampling rate could be more precisely controlled, this effect might be used to determine the true rpm.

One method that might have been successful in eliminating this effect would have been to use the system tachometer output in a control feedback loop to stabilize the motor speed. However, this would have required high tachometer stability. A more elegant and more practical method is to filter out the oscillations. Some success was achieved in this effort by taking a Discrete Fourier Transform (DFT) of the data, removing the low frequency oscillations, and performing the inverse transform. This work had to be terminated due to limited support for the effort, but preliminary results appeared promising.

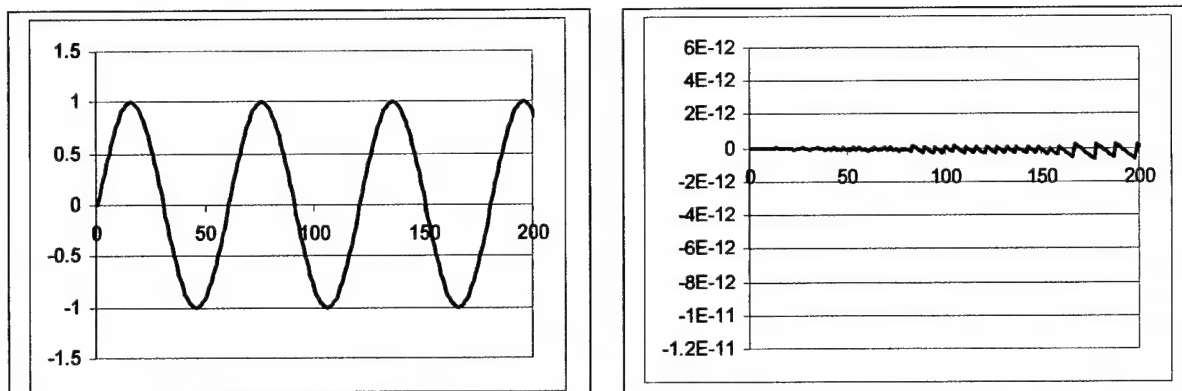


**Figure 35.** The sampling artifact of 1 second sampling on an eccentrically mounted rod rotating at 241 rpm (on the left) compared with a rod rotating at 240 rpm (on the right).

**3.3.3 Ambient load cell temperature** A third experimental artifact resulted from the temperature sensitivity of the load cell. Steam incident on the sample holder transfers heat to the test arm and from the test arm to the load cell. This effect is most clearly seen in Figures 30 and 31. To determine the magnitude of this effect, a thermocouple was mounted on the side of the load cell and the temperature and load cell output recorded as the sample holder of the test arm was exposed to steam inside the test chamber. In other words, the experimental configuration was identical to that encountered during friction and wear measurements in a steam environment. A typical example of the temperature induced force is shown in Figure 36 with a cubic least squares fit line. The load cell axis used to measure the normal force was used in this example. But the load cell configuration for measurement of the frictional force is similar to that for measurement of the normal force, as Figure 26 shows. Therefore, it was assumed that the temperature effect should be numerically the same for both.

An attempt was made to eliminate this temperature effect. The load cell was mounted on a water-cooled heat sink, and the measurement arm was thermally isolated from the load cell by ceramic spacers and ceramic mounting bolts. While this greatly reduced the magnitude of the effect, it did not eliminate it. An additional approach would be to fabricate an all ceramic or a composite arm with ceramic thermal spacers. Neither approach was practical under the limitations of the available funding. Instead, a numerical correction procedure was developed as described in the following subsection.



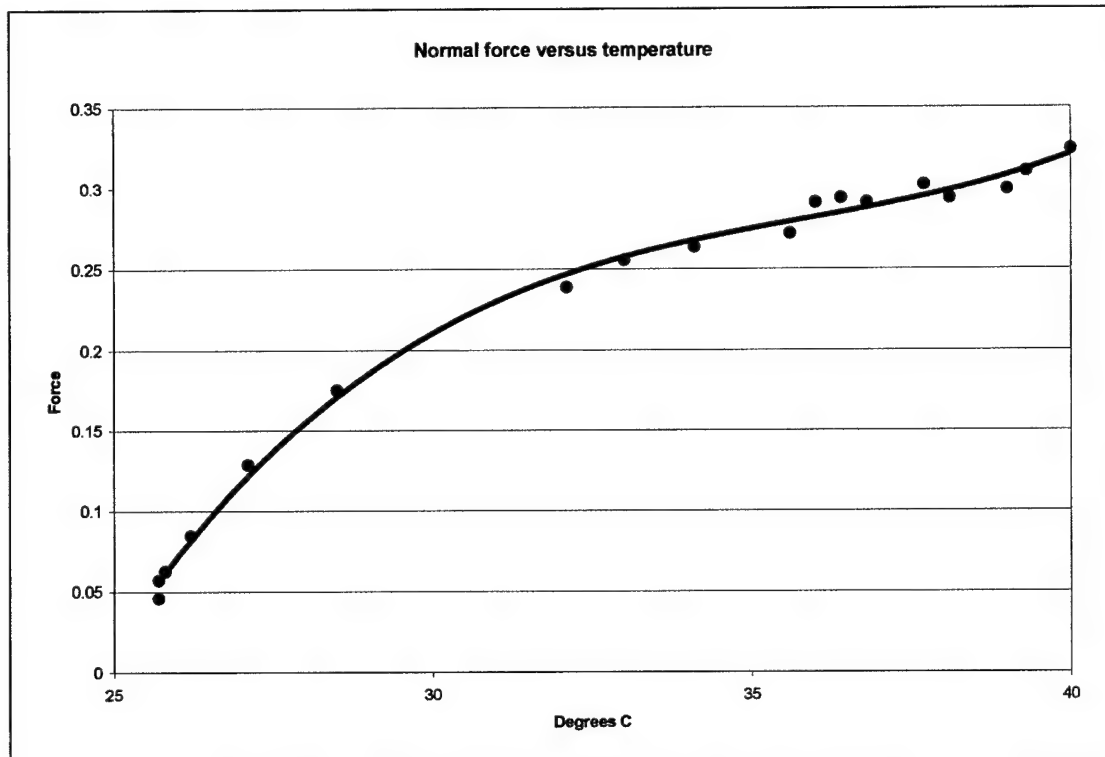


**Figure 36. Load cell force versus load cell temperature.**

**3.3.4 Temperature corrected data** The following procedure was used to correct data for the effects of temperature on the test arm and load cell.

**Step 1.** Record the difference between the normal force at some distance (or time) after steam flow was initiated and the normal force at the start of the experiment. This difference,  $\Delta F_N$ , is assumed to be entirely due to heating of the load cell.

**Step 2.** Since the temperature effect on the frictional force is assumed to be the same as that on the normal force, subtract  $\Delta F_N$  from the frictional force at the same distance (or time). This is the frictional force corrected for temperature effects on the test arm and load cell.

**Step 3.** The actual normal force should have been equal to the dead weight shown in Figure 30 as the "Applied Load".

**Step 4.** The coefficient of friction, COF, at the start of the experiment, "steam off", is the frictional force measured at the start of the experiment – no temperature effects – divided by the magnitude of the "Applied Load". The COF at some distance (or time) after the steam is applied is the frictional force corrected in Step 2 divided by the magnitude of the "Applied Load".

### **3.4 Friction and Wear Measurements**

**3.4.1 Sample acquisition and preparation** Materials were of two types: monolithic and coated substrates. Uncoated monolithic materials were alumina, titanium, Inconel-600, tungsten carbide, synthetic resin-impregnated carbon graphite (SGL Carbon EK 3245), and antimony-impregnated

carbon graphite (SGL Carbon EK 3205). Studies have indicated that these materials exhibit low friction surfaces and wear resistance in high-pressure, high-steam environments.<sup>29</sup> Coatings were as-deposited and annealed AlCuFe ternary quasicrystalline, boron carbide, and chrome nitride. Both rub blocks and rods were polished to a 1200 grit surface finish. Films of CrN, B<sub>4</sub>C, and AlCuFe were deposited by magnetron sputtering in a Sloan 1800 system. Annealing of the as-deposited AlCuFe films were performed at 500°C in air for periods of 2, 24, 48, and 110 hours, or in argon for 2, 24, and 48 hours. Couples of these materials that were used during this aspect of the program are listed in Table 3. The relative location of the rub block and rod are best seen in Figure 32 which shows the rub block attached to the measurement arm pressing against the rod. These are referred to as "Test Pieces" in that figure.

**Table 3. Material couples used during this effort**

Rub block		Rotating rod
<b>BASELINE MATERIALS</b>		
Resin bonded Gr		Al <sub>2</sub> O <sub>3</sub>
Resin bonded Gr		WC
Sb impregnated Gr		Al <sub>2</sub> O <sub>3</sub>
Sb impregnated Gr		WC
<b>UNCOATED METALS &amp; CERAMICS</b>		
Al <sub>2</sub> O <sub>3</sub>		Al <sub>2</sub> O <sub>3</sub>
Al <sub>2</sub> O <sub>3</sub>		WC
Ti		Ti
<b>COATED MATERIALS</b>		
Coating	Substrate	
AlCuFe QC	Al <sub>2</sub> O <sub>3</sub>	Al <sub>2</sub> O <sub>3</sub>
AlCuFe QC	Inconel	WC
AlCuFe QC	Ti	WC
Cr-CrN-B <sub>4</sub> C	Al <sub>2</sub> O <sub>3</sub>	Al <sub>2</sub> O <sub>3</sub>
Cr-CrN-B <sub>4</sub> C	Al <sub>2</sub> O <sub>3</sub>	WC
Cr-CrN-B <sub>4</sub> C	Ti	Al <sub>2</sub> O <sub>3</sub>
Cr-CrN-B <sub>4</sub> C	Ti	WC
Cr-CrN	Ti	WC
Cr-CrN	Al <sub>2</sub> O <sub>3</sub>	WC
Cr-CrN	Inconel	WC
Cr-CrN	Ti	WC

**3.4.2 Experimental conditions** Two environmental conditions were used. "Dry" indicates that the sample was maintained at room temperature and no steam was present. "Steam" indicates that steam was injected from the Sussman 3 kilowatt steam boiler directly onto the interface between the rub block and rotating rod. The temperature of this interface was measured to be close to 100°C, i.e., evaporative cooling was minimal.

During all measurements, the normal force, frictional force, COF, and wear were measured and recorded by the software shown in Figure 29. The applied normal force was maintain constant throughout while the frictional force, COF, and wear changed. However, plots of the normal force show that load cell did not record a constant force. In fact, the normal force at the rub block-rod interface was

<sup>29</sup> J. Kleemann und M. Woydt, "Friction in the millirange at 400°C without intrinsic solid Lubricants," Proc. 13th Int. Colloquium on Tribology, "Lubricants, Materials and Lubrication Engineering", 15.-17. January 2002, Ostfildern, Supplement, p. 37-51.

constant, but the actual force experienced by the load cell was not. This is explained, and the method of correction described, in the next section.

### 3.4.3 Measurement data

A typical set of tribological properties plots – normal force, frictional force, COF, and proximitor value – is shown in Figures 37a – d. Steam was turned on at about 275 meters and turned off at about 980 meters. These plots reveal that the temperature affected the normal force and, therefore, probably affected the frictional force as well. All raw, unprocessed data were reduced to this form and show the same general phenomena. The data was then corrected by the four-step procedure described above in Subsection 3.3.4. After correction, critical properties of the material couple were derived from the data for ease of comparison. These results are listed in Tables 4 and 5 and exhibited graphically in Figure 38 where the loads, 0.35 and 3.5 lbs., were chosen for the purpose of establishing a trend applicable to a steam engine environment. The extremes in a steam engine are represented by the high force of the scroll perimeter (or piston seal in some cases), and the relatively lower force of a heated journal bearing. Since the actual scroll perimeter force could not be reached by the Gardos Tribometer, results using these two forces were intended to indicate a friction and wear trend.

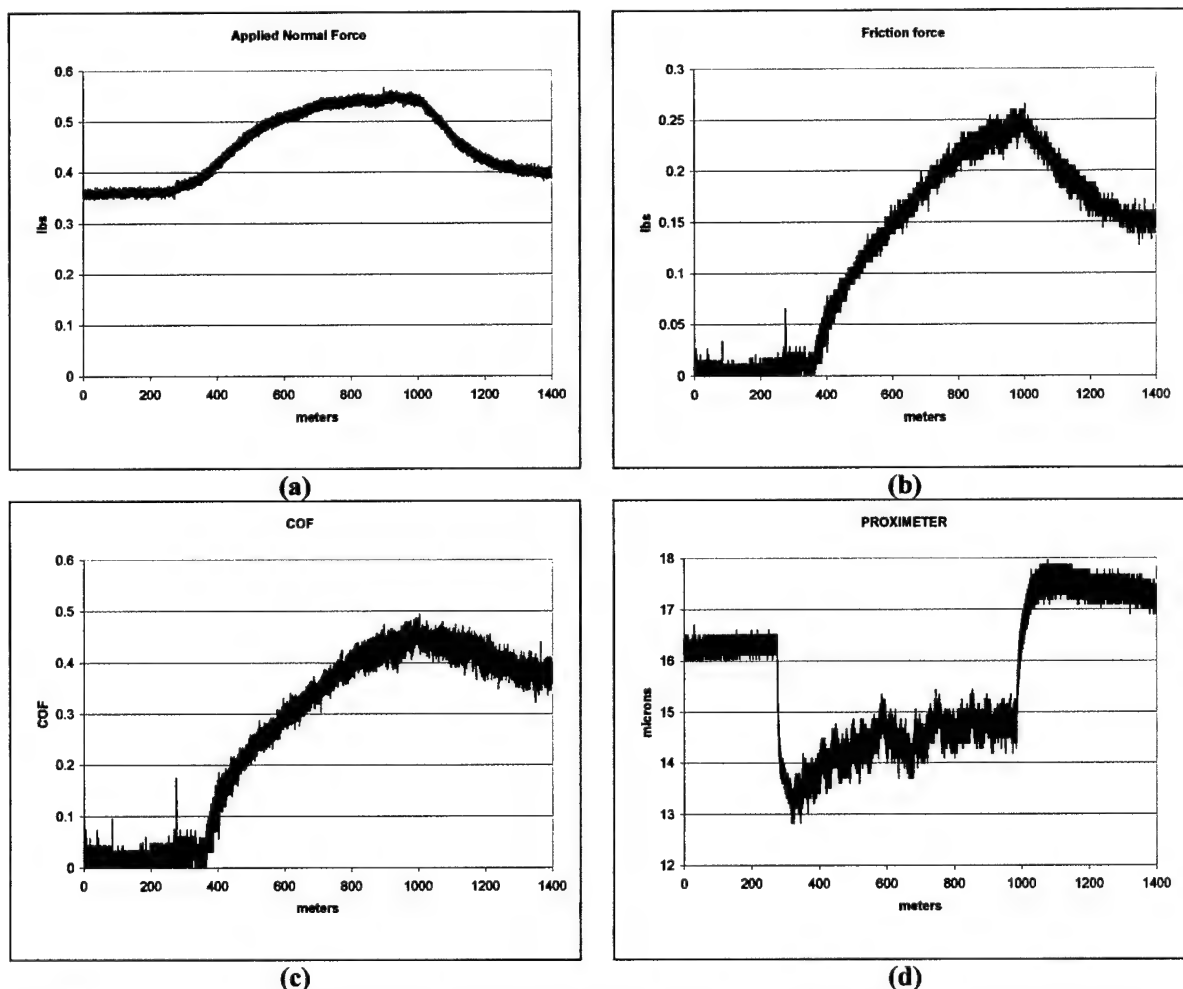


Figure 37 a – d. Typical uncorrected tribometer data – a) normal force, b) frictional force, c) COF, d) proximitor

**Table 4. Tribology measurement results (arranged by materials)**

MATERIAL COUPLES			MEASUREMENT RESULTS				
Rub block	Rotating rod	Normal force (lb)	COF		Wear (μm/m)		
			Dry	Steam	Dry	Steam	
UNCOATED COUPLES							
Resin bonded Gr	Al <sub>2</sub> O <sub>3</sub>	0.35	0.017	0.077	*	0.001	
Resin bonded Gr	Al <sub>2</sub> O <sub>3</sub>	3.5	0.15	0.15	0.002	0.01	
Resin bonded Gr	WC	0.35	0.175	0.034	-	-	
Resin bonded Gr	WC	3.5	0.148	0.022	*	0.004	
Sb impregnated Gr	Al <sub>2</sub> O <sub>3</sub>	0.35	0.08	<0.01	*	0.001	
Sb impregnated G	Al <sub>2</sub> O <sub>3</sub>	3.5	0.126	<0.01	*	0.002	
Sb impregnated Gr	WC	0.35	0.1	<0.01	<0.002	<0.002	
Sb impregnated G	WC	3.5	0.169	<0.01	0.001	0.007	
Al <sub>2</sub> O <sub>3</sub>	Al <sub>2</sub> O <sub>3</sub>	0.35	*	0.14	-	<0.01	
Al <sub>2</sub> O <sub>3</sub>	WC	0.35	0.24	<0.01	*	-	
Ti	Ti	3.5	0.323	-	0.01	-	
COATED COUPLES							
Coating	Substrate						
AD QC	Al <sub>2</sub> O <sub>3</sub>	Al <sub>2</sub> O <sub>3</sub>	0.35	1.53	0.054	-	0.003
AD QC	Inconel	WC	0.35	0.75	0.6	0.0013	0.0013
AD QC	Ti	WC	0.35	0.521	<0.01	0.001	0.002
AN QC	Al <sub>2</sub> O <sub>3</sub>	WC	0.35	-	1.54	-	0.045
AN QC	Inconel	WC	0.35	-	0.2	-	0.02
AN QC	Ti	WC	0.35	-	1.73	-	0.03
B <sub>4</sub> C	Ti	Al <sub>2</sub> O <sub>3</sub>	0.35	0.041	<0.01	0.57	0.005
B <sub>4</sub> C	Ti	WC	0.35	<0.01	<0.01	-	0.025
Cr-CrN	Ti	WC	0.35	0.143	<0.01	-	-
Cr-CrN	Al <sub>2</sub> O <sub>3</sub>	WC	0.35	-	0.209	-	0.009

**Notes:**

\* indicates very low wear rate, - indicates unreliable data

QC = AlCuFe quasicrystalline thin film

AD = as deposited, AN = annealed

All B<sub>4</sub>C were deposited on top of a Cr-CrN bond layer

**Table 5. Tribology measurement results (arranged by COF in steam)**

MATERIAL COUPLES			MEASUREMENT RESULTS			
Rub block Coating/Substrate		Rotating rod	Normal force (lb)	COF		Wear (µm/m)
				Dry	Steam	Dry      Steam
<b>VERY GOOD (steam COF &lt;0.01)</b>						
Sb impregnated Gr		Al <sub>2</sub> O <sub>3</sub>	0.35	0.08	<0.01	*      0.001
Sb impregnated G		Al <sub>2</sub> O <sub>3</sub>	3.5	0.126	<0.01	*      0.002
Sb impregnated Gr		WC	0.35	0.1	<0.01	<0.002      <0.002
Sb impregnated G		WC	3.5	0.169	<0.01	0.001      0.007
Al <sub>2</sub> O <sub>3</sub>		WC	0.35	0.24	<0.01	*      -
B <sub>4</sub> C	Ti	Al <sub>2</sub> O <sub>3</sub>	0.35	0.041	<0.01	0.57      0.005
B <sub>4</sub> C	Ti	WC	0.35	<0.01	<0.01	-      0.025
Cr-CrN	Ti	WC	0.35	0.143	<0.01	-      -
AD QC	Ti	WC	0.35	0.521	<0.01	0.001      0.002
<b>GOOD (0.01 &lt; steam COF &lt;0.1)</b>						
Resin bonded Gr		WC	3.5	0.148	0.022	*      0.004
Resin bonded Gr		WC	0.35	0.175	0.034	-      -
AD QC	Al <sub>2</sub> O <sub>3</sub>	Al <sub>2</sub> O <sub>3</sub>	0.35	1.53	0.054	-      0.003
Resin bonded Gr		Al <sub>2</sub> O <sub>3</sub>	0.35	0.017	0.077	*      0.001
<b>POOR (1 &lt; steam COF &lt;0.1)</b>						
Al <sub>2</sub> O <sub>3</sub>		Al <sub>2</sub> O <sub>3</sub>	0.35	*	0.14	-      <0.01
Resin bonded Gr		Al <sub>2</sub> O <sub>3</sub>	3.5	0.15	0.15	0.002      0.01
AN QC	Inconel	WC	0.35	-	0.2	-      0.02
Cr-CrN	Al <sub>2</sub> O <sub>3</sub>	WC	0.35	-	0.209	-      0.009
AD QC	Inconel	WC	0.35	0.75	0.6	0.0013      0.0013
<b>VERY POOR (1 &lt; steam COF)</b>						
Ti		Ti	3.5	0.323	-	0.01      -
AN QC	Al <sub>2</sub> O <sub>3</sub>	WC	0.35	-	1.54	-      0.045
AN QC	Ti	WC	0.35	-	1.73	-      0.03

**Notes:**

\* indicates very low wear rate, - indicates unreliable data

QC = AlCuFe quasicrystalline thin film

AD = as deposited, AN = annealed

All B<sub>4</sub>C were deposited on top of a Cr-CrN bond layer

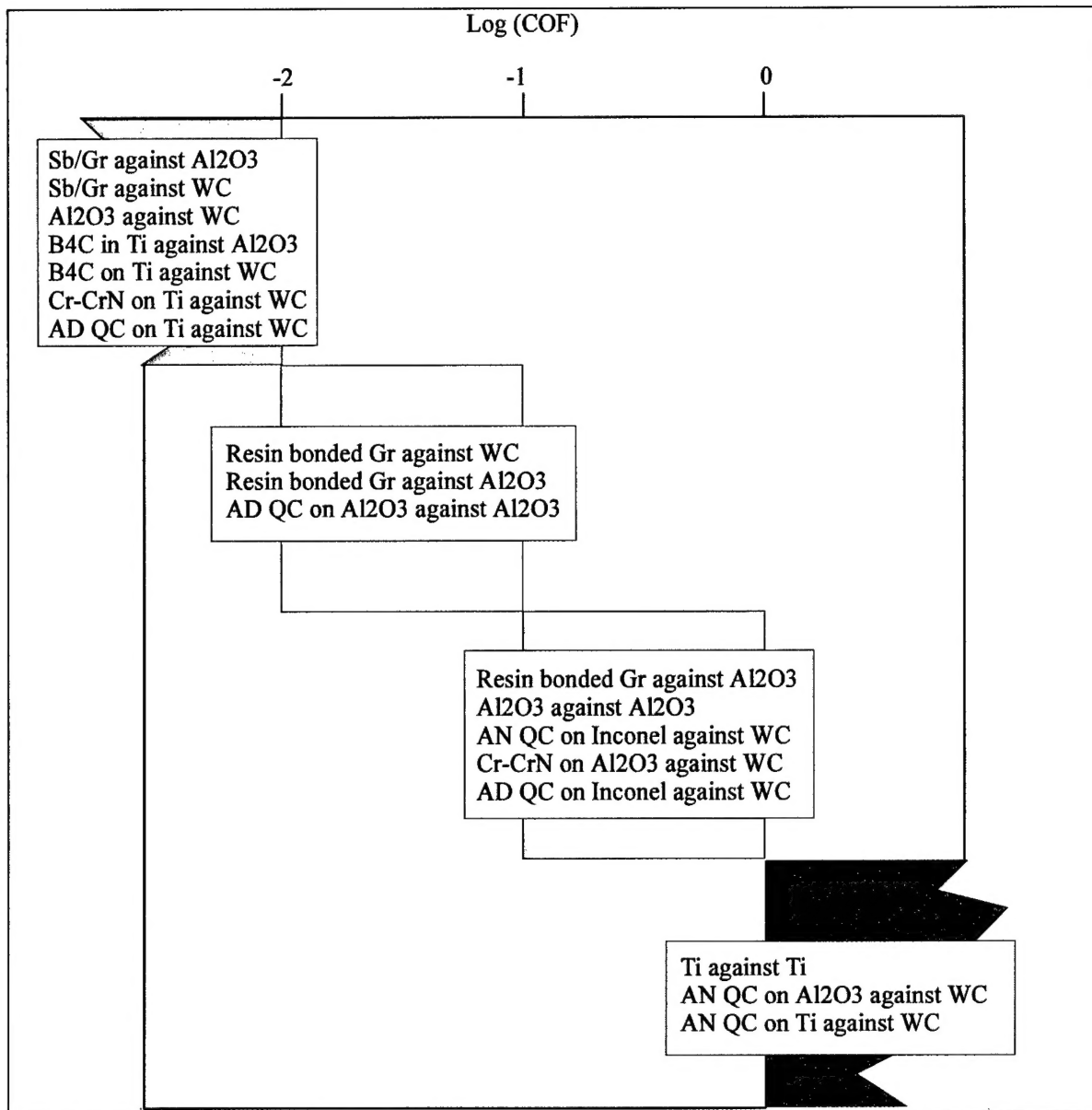


Figure 38. Tribology measurements arranged by COF

**3.4.4 Steam tribometry conclusions** The Sb-impregnated graphite exhibited the lowest COF at both loads and against both Al<sub>2</sub>O<sub>3</sub> and WC substrates. These results are consistent with previous German steam engine testing at Enginon in Berlin. A similar Sb-impregnated rotor running against a hard 2.5 wt % MgO-ZrO<sub>2</sub> fixed counterface produced a COF of 0.01 in 650°C steam.<sup>30</sup> The resin bonded graphite without Sb exhibited a COF between 2 and 10 times higher. Surprisingly, the hardest and most dissimilar couple, Al<sub>2</sub>O<sub>3</sub> against WC exhibited equally low COF under the lighter load as did one as-deposited QC film on Ti when run against WC. In fact, all except one of the films on Ti run against either WC or Al<sub>2</sub>O<sub>3</sub> exhibited COFs comparable to the best results obtained from the two different graphite systems. That cannot be attributed to the hardness of the substrate because a Cr-CrN film on

<sup>30</sup> Fehrenbacher, L., "Trip Report, Technology Assessment & Transfer", Sept. 9, 2002.

Al<sub>2</sub>O<sub>3</sub> run against WC exhibited one of the highest COFs while the same coating system on the relatively softer Ti substrate exhibited one of the lowest COFs. Not surprising, was that Ti run against Ti and Al<sub>2</sub>O<sub>3</sub> run against Al<sub>2</sub>O<sub>3</sub> both exhibited some of the highest COFs measured. This was expected since galling would dominate the wear mechanism. The same general behavior is always observed when identical materials are used. For example, SS 304 run against SS 304 and alumina bronze run against aluminum bronze always exhibited severe galling, high COFs, and high wear rates.

In cases that good wear data could be obtained, low wear rates were generally found for dissimilar materials. Very high wear rates often were associated with film failure and/or debonding. To show that coatings are not a viable solution to the steam engine wear problem, consider the requirements of a coated scroll tip and perimeter seal. At 15,000 rpm the scroll will make  $9 \times 10^8$  rotation in 1000 hours – a reasonable lifetime expectation. This corresponds to  $4.3 \times 10^8$  meters of tip travel for a 6" diameter scroll. Assuming a maximum coating thickness of 10  $\mu$ m, the wear rate must not exceed  $2.3 \times 10^{-8}$   $\mu$ m/m. The data tabulated above shows that typical wear rates *for the loads that were used* are typically 5 orders of magnitude too large! It is clear that only in situ engine life tests will provide meaningful wear data for these systems.

#### 4. PROGRAM SUMMARY CONCLUSIONS

Significant progress was made towards an understanding of phase development and oxidation in the AlCuFe quasicrystalline system. Microstructure analysis by synchrotron diffraction exhibited the route for phase formation from the as-deposited precursor films. Formation of the R-phase occurred at 450°C, below the previously published value of 475°C. Preferential oxidation occurs in the near-surface region and temporarily disrupts formation of the R-phase microstructure, despite encapsulation in argon atmosphere. Fluctuation microscopy and other structural analysis showed the presence of an ordered, polycrystalline oxide on the surface of AlCuFe films annealed at 500°C to 600°C. This oxide film appeared to consist of aluminum oxide, and lacked copper and iron. The combination of microstructure analysis, phase development on annealing, and analysis of the oxide phase provided fundamental understanding of AlCuFe quasicrystalline coatings in steam engine applications. A tribological testing system capable of operating in a high temperature, steam environment was modified and tested. Room ambient and 100°C steam testing of Sb-impregnated graphite-hard ceramic combinations supported the high temperature steam test results at Enginon.

#### 5. PUBLICATIONS

The following publications were produced during the course of this research.

M.J. Daniels, D. King, L. Fehrenbacher, J.S. Zabinski, J.C. Bilello, Physical Vapor Deposition Route for Production of AlCuFeCr and AlCuFe Quasicrystalline and Approximant Coatings, Submitted to *Surface and Coatings Technology* (September 2003).

M. J. Daniels, Benjamin Phillips, D. King, J.S. Zabinski, and J.C. Bilello, Nature of the As-Deposited State in AlCuFeCr PVD Coatings, *Thin Solid Films* 440 (1-2), (2003) 87.

M. J. Daniels, Doctoral Dissertation, "Phase, Microstructure, and Chemistry of AlCuFeCr and AlCuFe Quasicrystalline Wear Coatings Produced via Physical Vapor Deposition," The University of Michigan (2003).

M. J. Daniels, D. King, J.S. Zabinski, and J.C. Bilello, Intermediate Annealing Behavior and Grain Growth of AlCuFe Quasicrystalline Coatings, Presented at the *Materials Research Society Fall Meeting* (December 2002) W12.7.

M. J. Daniels, B. L. French, D. King, and J.C. Bilello, In situ Fracture and Adhesion Failure of AlCuFe Quasicrystalline Films, Presented at the *Materials Research Society Fall Meeting* (December 2002) Y3.3.